Submitted to Int. J. Mass Spectrom. (H. Schwarz Honor Issue)

Sequential Activation of Methane by Ir^+: An IRMPD and Theoretical Investigation

Oscar W. Wheeler,[†] Michelle Salem,[†,‡] Amanda Gao,[†,‖] Joost M. Bakker,[§] and P. B. Armentrout[*,†]

[†]*Department of Chemistry, University of Utah, 315 S. 1400 E. Room 2020, Salt Lake City, Utah 84112, United States*

[§]*Radboud University, Institute for Molecules and Materials, FELIX Laboratory, Toernooiveld 7c, 6525ED Nijmegen, The Netherlands*

[‡]*Present address: Department of Chemistry and Biochemistry, California State University San Marcos, 333 S. Twin Oaks Valley Rd., San Marcos, California 92096, United States*

[‖]*Present address: Department of Chemistry and Chemical Engineering, California Institute of Technology, 1200 E. California Boulevard, Pasadena, California 91125, United States*

Abstract:

The sequential activation of up to 4 CH_4 molecules by Ir^+ is investigated through a gas-phase infrared multiple photon dissociation (IRMPD) experiment and theoretical calculations. A molecular beam apparatus was used to generate Ir^+ by laser ablation and expose it to controlled amounts of CH_4. Product ions were irradiated with IR light from a free electron laser over the 500 – 1800 cm^{-1} spectral range and photodissociation was monitored using a time-of-flight mass spectrometer. Experimental spectra were obtained for five distinct species: $[Ir,3C,8H]^+$, $[Ir,3C,10H]^+$, $[Ir,4C,10H]^+$, $[Ir,4C,12H]^+$, and $[Ir,O,3C,12H]^+$. To identify these species, B3LYP/def2-TZVPPD geometry optimizations were performed on a variety of possible structures, with computed IR spectra compared to the experimental IRMPD spectra. This has led to the following assignments: $[Ir,3C,8H]^+ = IrCH_2(CH_3)_2^+$, $[Ir,3C,10H]^+ = HIr(CH_3)_3^+$, $[Ir,4C,10H]^+ = Ir(CH_3)_2(C_2H_4)^+$, $[Ir,4C,12H]^+$ = a mixture of $HIr(CH_3)(C_2H_4)^+(CH_4)$, $HIr(CH_3)_2(C_2H_5)^+$,

$Ir(CH_3)_4^+$, and $(H_2)Ir(CH_3)_2(C_2H_4)^+$, and $[Ir,O,3C,12H]^+ = (H_2O)HIr(CH_3)_3^+$. Notably, evidence for C-C coupling is observed upon reaction with a fourth methane. Mechanisms for the formation of the observed products were also explored computationally by examining the reaction coordinate pathways for the reactions of methane with $HIrCH^+$, $IrCH_2^+$, $Ir(CH_3)_2^+$, $HIrCH_2(CH_3)^+$, $HIr(CH_3)_3^+$, and $IrCH_2(CH_3)_2^+$.

Keywords: methane activation; infrared multiple photon dissociation; iridium; carbon-carbon coupling; dehydrogenation; reaction coordinate pathway

1. Introduction

The natural abundance of small alkanes coupled with both the demand for and finite supply of fossil fuels has provided the foundation for great interest in the catalytic activation of hydrocarbons by transition metals [1]. By examining these processes in the gas-phase, the fundamental steps that make up such catalytic activity can be explored at their most basic level, with particularly notable contributions by Schwarz[2, 3]. Such gas-phase work can provide a foundation to elucidate periodic trends, reaction efficiencies, and reaction pathways [2-5].

Armentrout has recently reviewed experimental results examining periodic trends in the reaction of methane with atomic 5d transition-metal cations, including detailed reaction energetics [5]. Among these results, the reaction of $Ir^+ + CH_4$ is highly efficient as characterized in a number of experimental studies including Fourier transform ion cyclotron resonance (FTICR) mass spectrometry [6, 7], guided ion beam tandem mass spectrometry (GIBMS) [8], and inductively coupled plasma/selected ion flow tube (ICP/SIFT) mass spectrometry [9]. GIBMS studies report reaction efficiencies of 99 ± 20% (CH_4) [8] compared to the Langevin-Gioumousis-Stevenson (LGS) collision rate [10], similar to that of Os^+ (100 ± 20%) [11] and double that of Pt^+ (50 ± 10%) [12]. The FTICR [6, 7] and ICP/SIFT [9] studies reported efficiencies for methane activation by Ir^+ of 71 ± 25 % and 100 ± 30 %, respectively.

Despite extensive work on the activation of methane by atomic transition metal cations, the structural characterization of the products formed in these reactions is limited within the literature. Previously, Lapoutre *et al.* investigated the $[M,C,2H]^+$ products formed by the reaction of $M^+ + CH_4$, where M = Ta, W, Ir, and Pt, using infrared multiple photon dissociation (IRMPD) spectroscopy [13]. This IRMPD spectroscopy study was performed with a molecular beam apparatus and irradiation from the Free-Electron Laser for IntraCavity Experiments (FELICE) beamline at the Free-Electron Lasers for Infrared eXperiments (FELIX) laboratory [14]. By comparing experimental spectra of these species with vibrational spectra generated from theoretical calculations, structures of the $[M,C,2H]^+$ ions could be identified. Only the $[Pt,C,2H]^+$ species spectrum was assigned solely to the classic C_{2v} carbene structure. The $[Ta,C,2H]^+$ and

$[W,C,2H]^+$ species exhibit distorted carbene structures resulting from agostic interactions. The $[Ir,C,2H]^+$ product showed evidence of multiple structures, consistent with B3LYP/def2-TZVPPD theoretical calculations that indicate two products can be formed exothermically by reaction of Ir^+ with CH_4. The $^1A'$ carbyne hydride, $HIrCH^+$, is the ground state structure and its spectrum dominated the experimental spectrum. Contributions were also evident from the $^3A_2$ C_{2v} carbene, $IrCH_2^+$, 0.25 eV higher in energy but still 0.58 eV lower in energy than the Ir^+ (^5F) + CH_4 reactants. Notably, both products are formed in reactions that do not conserve spin. Verification of these assignments has been achieved by examination of the analogous perdeuterated species, $[M,C,2D]^+$, where the importance of including rotational band structure to reproduce the experiment was also demonstrated [15]. Extensions of this work now confirm that the $[Os,C,2H]^+$ species formed in methane activation by Os^+ also has the carbyne hydride structure, but now with no indications of carbene present [16].

There are a greater number of studies within the literature that investigate vibrational spectroscopy of atomic metal and small metal cluster cations complexed with methane: $Li^+(CH_4)_{1-9}$ and $Li^+(CH_4)Ar_{1-6}$ [17, 18], $Al^+(CH_4)_{1-6}$ [19], $Mn^+(CH_4)_{1-6}$ [20], $Fe^+(CH_4)_{1-4}$ [21], $Fe_2^+(CH_4)_{1-3}$ [22], $Co^+(CH_4)_{1-4}$ [23], $Ni^+(CH_4)_{1-4}$ [23], $Cu^+(CH_4)_{1-6}$ [24], $Ag^+(CH_4)_{1-6}$ [24], and $Pt_{3-5}^+(CH_4)(Ar)$ [25]. In all of these cases, the methane ligands are intact and no C-H bond activation has occurred. A recent study reports evidence for the formation of $H\text{-}Au_{2-4}^+\text{-}CH_3$ upon reacting with Au_{2-4}^+ clusters with methane at room temperature, although methane adducts remain the dominant species formed [26].

In a study parallel to the present investigation, the sequential activation of multiple methane molecules by Pt^+ was examined by IRMPD spectroscopy using a molecular beam apparatus coupled to the conventional FELIX beamline [27]. Comparisons between computational and experimental IR spectra indicated that Pt^+ was capable of activating two methane molecules. Although only a single dehydrogenation takes place in the formation of $PtCH_2^+$, IRMPD results show that $PtCH_2^+$ activates a second CH_4 molecule to form $Pt(CH_3)_2^+$, which could then coordinate with two more intact CH_4 ligands. These results are consistent with previous FTICR results [6] that show that Pt^+ rapidly reacts with only a single CH_4 molecule. In contrast, FTICR results find that Ir^+ undergoes two fast reactions with methane and up to three total reactions to give $[Ir,3C,6H]^+ + 3\ H_2$ [6]. Because the previous IRMPD studies show that $[Pt,C,2H]^+$ and $[Ir,C,2H]^+$ have different structures, this change in sequential reactivity could be a consequence of the different structural precursors. It is the purpose of the present study to examine the sequential reactions of Ir^+ with multiple CH_4 molecules, using IRMPD spectroscopy and the same experimental setup as the previous work on the Pt^+ system. Structures associated with the sequential reactions of Ir^+ and three and four molecules of CH_4 are assigned along with that for a serendipitously produced water complex. The present work also offers theoretical insight into the reaction mechanisms that are required for the formation of the assigned product structures.

2. Experimental and Computational Methods

2.1. Experiment

The experiments performed here used a molecular beam apparatus, previously described [28], coupled to the conventional IR [29] beam line at FELIX. A brief description of the experimental setup follows. Ir^+ ions were generated by ablating an Ir sample using the second harmonic of a pulsed Nd:YAG laser. A pulse of helium cooled the ions and transported the beam through a 3 mm diameter and 60 mm long channel. Further downstream, the reactant gas was introduced into the molecular beam as a methane/helium mixture (~1:5), which led to reactions of CH_4 molecules with Ir^+. The extent of reaction between CH_4 and Ir^+ was manipulated by varying the length of the reactant CH_4 gas pulse. The reactive mixture containing $[Ir,xC,yH]^+$ products, was expanded into vacuum forming a molecular beam that was collimated by a 2 mm diameter skimmer and then a 1 mm diameter aperture, both of which were electrically grounded. The aperture effectively shaped the molecular beam for maximum interaction with IR laser pulses from the FELIX beamline on alternate pulses. All ions formed in the source and product ions resulting from irradiation were extracted into an orthogonal reflectron time-of-flight (RTOF) mass spectrometer (mass resolution ~ 1700) [28] and detected with a microchannel plate detector.

Irradiation from FELIX used macropulses of 10 μs with a repetition rate of 10 Hz. The macropulses can reach a power of 100 mJ and were composed of picosecond long pulses spaced by 1 ns with a bandwidth that is adjustable to 0.2 – 1.0 % root-mean-square of the selected frequency. An important difference between FELIX and FELICE is the macropulse power, where FELICE can reach power levels of 2 J in the laser cavity [29].

Two sets of mass spectra were generated: without and with IR exposure, from which mass channel intensities I_{ref} and $I_{sig}(v)$, respectively, were extracted. The spectral responses of mass channels of interest were interpreted in two distinct modes: depletion and growth. The depletion yield was calculated by taking the negative logarithm of $I_{sig}(v)/I_{ref}$ at the same mass-to-charge ratio (*m/z*) and is proportional to the cross section for photodissociation [30]. The growth yield was obtained from $-\ln[I_{sig,\mathrm{P}}/(I_{sig,\mathrm{P}} + I_{sig,\mathrm{F}} - I_{ref,\mathrm{F}})]$ where P represents precursor ions and F are fragment ions. For both depletion and growth modes, the obtained yields were corrected for laser power fluctuations and the wavelength was calibrated using a grating spectrometer.

2.2 Quantum Chemical Calculations

In the present study, structural elucidation is achieved through comparisons of experimental spectra with vibrational frequencies calculated for likely structures using density functional theory (DFT). The present work utilized Gaussian09 [31] for all quantum chemical calculations, which were performed on the workstations of the Center for High Performance Computing (CHPC) at the University of Utah. The current results utilized the same approach as some of the previous IRMPD study of $Pt^+ + x\ CH_4/CD_4$ reactions [27] and a similar approach as that of Lapoutre *et al.* [13] in their IRMPD study of the 5d transition metal $M^+ + CH_4$ reactions. Geometry optimizations were performed with the B3LYP hybrid functional [32, 33] and the def2-TZVPPD basis set [34], which is a balanced triple-ζ valence basis set with double polarization and diffuse functions on all elements. The Stuttgart-Dresden small-core effective core potential (ECP), commonly abbreviated SDD, was used for the Ir atom [34], so that its 5s, 5p, 6s, 6p, and 5d electrons are explicitly treated. Additional single point energy calculations were performed at the MP2(full)/def2-TZVPPD level of theory (where full indicates all electrons are included in the correlation) using the B3LYP/def2-TZVPPD optimized geometries. B3LYP total energies, zero-point energies, and symmetries along with MP2 energies are reported in the Supporting Information in Table S1. All reported single point energies include corrections for zero-point energies (with frequencies scaled by 0.9885) [35]. Future references within the text to these B3LYP/def2-TZVPPD and MP2(full)/def2-TZVPPD//B3LYP/def2-TZVPPD single point energies will be abbreviated as B3LYP and MP2, respectively.

Comparisons between experimental and theoretically generated spectra occur after convoluting the theoretical spectra with a Gaussian line shape having a width of 20 cm^{-1} (fwhm ≈ 50 cm^{-1}). The theoretical frequencies were scaled to help account for deficiencies in the calculated vibrations, anharmonicities, and multiphoton effects. In previous work, FELICE results for $[Ir,C,2H]^+$ used a scaling factor of 0.939 [13], whereas the $Pt^+ + x\ CH_4$, $x = 1 – 4$, FELIX study used a scaling factor of 0.983 to get the best overlap with theoretical results [27]. The present work favors a scaling factor of 0.955 to most effectively reproduce the experimental spectra.

Comparison of the experimental and theoretical spectra provides tentative assignments of the structures of several species, as described below. Validation of these assignments can be accomplished by understanding the processes required for forming these products. Therefore, reaction coordinate pathways (RCPs) were calculated to elucidate the processes required for formation of the assigned structures of the experimental spectra. These reaction pathways used B3LYP/def2-TZVPPD geometry optimizations and zero-point energy corrected B3LYP and MP2 single point energies with the def2-TZVPPD basis set. These were calculated for both singlet and triplet surfaces, whereas quintet spin RCPs were not investigated because of the much higher energies associated with these species.

To validate this theoretical approach, we calculated thermochemistry for H_2, CH, CH_2, CH_3, and CH_4 along with the iridium species, IrH^+, IrC^+, $IrCH^+$, $IrCH_2^+$, and $IrCH_3^+$ at both the

B3LYP and MP2 levels. Experimental thermochemistry for comparison was taken from the literature [36] and our previous study of the reactions of Ir^+ with methane [8]. Details of these calculations can be found in Table S2 of the Supporting Information. Both levels of theory reproduce the thermochemistry for H_2 and CH_x with mean absolute deviations (MAD) of 0.04 (B3LYP) and 0.14 (MP2) eV. The iridium species were also nicely reproduced by the B3LYP calculations, with a MAD of 0.18 eV and a maximum error of 0.36 eV. In contrast, the MP2 calculations had a MAD of 0.65 eV with large overbinding found for the multiply bound IrC^+ (1.63 eV larger than experiment) and $IrCH^+$ (1.27 eV larger than experiment). As the species considered in the present study generally involve multiple bonds to iridium, the B3LYP calculations are used exclusively in the discussion below to evaluate the mechanisms for reaction.

All energy values within this work are reported at 0 K, consistent with previous IRMPD work [13, 15, 16, 27]. To verify that relative 298 K Gibbs energies should not differ significantly from these values, the Gibbs energies for five $[Ir,3C,10H]^+$ isomers were explicitly calculated. These results showed that relative 298 K Gibbs energies do not change the energetic order, with values changing by only 0.02 – 0.10 eV.

3. Experimental Results

The reaction of $Ir^+ + x\ CH_4$, where $x = 1 – 4$, produces a number of different product ions. Assignment of the various *m/z* peaks is complicated by the isotopic distribution of Ir, which has isotopes at 191 (37.3%) and 193 (62.7%) [37]. Contributions from ^{13}C species are not considered in the present analysis because even for the reaction of Ir^+ with 4 CH_4, the likelihood of 0, 1, 2, 3, and 4 ^{13}C species is 96.1, 3.9, and < 0.01 %, respectively. An example mass spectrum of the $Ir^+ + x\ CH_4$ products with and without exposure to 1015 cm^{-1} irradiation is shown in Fig. 1. A list of likely molecular formulas for all observed mass channels can be found in Table S3.

Assignment of these mass spectral peaks can be achieved through knowledge of the isotopic distribution coupled with verification by the spectroscopic results and reaction pathways. In Fig. 1, there are 3 distinct groups of peaks that are populated by products of the $Ir^+ + x\ CH_4$

reactions, where $x = 2 – 4$. Minor amounts of $[Ir,C,2H]^+$, $m/z = 205$ and 207, were observed but show no noticeable growth or depletion associated with FEL exposure over the explored wavelength range. The $x = 2$ group of products has m/z peaks at 219, 221, and 223. The 223 m/z channel is composed solely of the $[^{193}Ir,2C,6H]^+$ species corresponding to a single dehydrogenation of two methane molecules. The 221 m/z channel has a mixture of the $[^{191}Ir,2C,6H]^+$ and $[^{193}Ir,2C,4H]^+$ species and the m/z 219 channel is solely composed of the $[^{191}Ir,2C,4H]^+$ species, which represents a double dehydrogenation process that is about 1.5 times as intense as the single dehydrogenation process. The $x = 3$ group of peaks without irradiation also appears as a triplet at m/z 235, 237, and 239, again associated with both single and double dehydrogenation. Unlike the less intense $x = 2$ group, the intensities suggest that the single dehydrogenation dominates over the double dehydrogenation, but only by a 6:5 ratio. The m/z 239 channel is composed of the $[^{193}Ir,3C,10H]^+$ species; the m/z 237 channel is a mixture of the $[^{191}Ir,3C,10H]^+$ and $[^{193}Ir,3C,8H]^+$ species in about a 5:7 ratio; and the m/z 235 channel is composed dominantly by the $[^{191}Ir,3C,8H]^+$ species. Finally, the $x = 4$ group without irradiation also has a triplet of masses at m/z 249, 251, and 253, with small peaks at m/z 255 and 257. The isotopic ratios allow the following assignments: m/z 253 = $[^{193}Ir,4C,12H]^+$ (minor amount of $[^{191}Ir,4C,14H]^+$), 251 = $[^{191}Ir,4C,12H]^+$ and $[^{193}Ir,4C,10H]^+$, and 249 = $[^{191}Ir,4C,10H]^+$. Note that the dominant reactions here are double and triple dehydrogenations of four methane molecules, in a ratio of 1:2.2. The small peaks observed at m/z 255 and 257 are attributed to a small water contaminant within the system for both masses: 257 = $[^{193}Ir,O,3C,12H]^+$ and 255 = $[^{191}Ir,O,3C,12H]^+$ along with some minor contribution from the $[^{193}Ir,4C,14H]^+$ species, the single dehydrogenation product. This contribution is needed to explain why m/z 255 has a higher intensity than m/z 257. Low intensity products were also observed in the $x = 5$ m/z range but were not been investigated further in the current work because of mass overlap and additional water contamination.

Depletion and growth yields for the aforementioned $x = 2 – 4$ products can be seen in the Supporting Information, Figs. S1 – S4, along with further discussion on how elemental compositions were assigned on the basis of isotopic distributions. Table S4 of the Supporting Information lists the processes observed and the possible pathways for these processes. From this analysis, we conclude that spectra could be obtained for five unique molecular species. Depletion spectra obtained for *m/z* 239, 253, and 257 correspond to $[^{193}\text{Ir,3C,10H}]^+$, $[^{193}\text{Ir,4C,12H}]^+$, and $[^{193}\text{Ir,O,3C,12H}]^+$ molecular species, respectively. Growth spectra are also examined for the *m/z* 219 and 233 channels and can be attributed to CH_4 loss from $[^{191}\text{Ir,3C,8H}]^+$ (*m/z* 235) and $[^{191}\text{Ir,4C,10H}]^+$ (*m/z* 249), respectively. The growth spectrum for *m/z* 247 (dehydrogenation of *m/z* 249) may be used interchangeably with the *m/z* 233 spectrum but has increased noise. The *m/z* 231 channel was not explored further because it can be assigned to minor secondary dissociation process from either *m/z* 233 or 247, Table S4.

4. Comparisons of Theoretical Results to Experimental Spectra

Structures for the five species of interest were explored theoretically for spin multiplicities of 1, 3, and 5 (only 1 for $[\text{Ir,O,3C,12H}]^+$) to ensure a thorough investigation of possible isomers. In general, the most stable systems have several covalent bonds formed through the activation of CH_4, and therefore have spin multiplicities of 1, whereas the 3 and 5 multiplicity counterparts are typically higher in energy. In a few instances (specifically mentioned below), calculations from the current work were unable to find stable geometries for a specific spin multiplicity despite our best efforts.

4.1. Spectrum and Structures of $[\text{Ir,3C,10H}]^+$

The depletion spectrum of the *m/z* 239 channel and the growth spectrum of the *m/z* 223 channel are nearly identical, indicating that *m/z* 239 loses a methane molecule to form *m/z* 223. Thus, these spectra correspond to a species with the molecular formula $[^{193}\text{Ir,3C,10H}]^+$ in which a single dehydrogenation of three methane molecules has occurred. The *m/z* 239 channel is a clean experimental spectrum originating from a single Ir isotope. Forty unique isomers (fifteen different structural motifs) were examined computationally for comparison with the experimental spectrum.

Table 1 provides a list of the B3LYP relative energies of all structures in Fig. 2, whereas a more comprehensive list of relative energies can be found in Table S5 of the Supporting Information and includes MP2 values. These structures have a variety of binding motifs including activation of all three CH_4 molecules: $HIr(CH_3)_3^+$_trans, $HIr(CH_3)_3^+$_cis, and $(H)_2IrCH_2(CH_3)_2^+$. Relative energy comparisons suggest that the $HIr(CH_3)_3^+$_trans structure is the ground structure (GS) for B3LYP calculations and is 0.07 eV above the MP2 GS, Table S5. The "trans" designation specifies the orientation of the methyl groups and has three H-Ir-C-H dihedral angles of 180º; the "cis" configuration (at 0.29eV) has dihedral angles of 0º. Additional binding motifs include formation of C-C bonds in seven unique structures with $(H)_2Ir(C_2H_4)^+(CH_4)$ being the GS for MP2 calculations (0.18 eV above the B3LYP GS). In Table S5, both $(H)_2Ir(CHCH_3)^+(CH_4)$ and $HIrC_2H_5^+(CH_4)$ are less than 0.5 eV above the GS for both B3LYP (0.41 and 0.49 eV) and MP2 (0.45 and 0.22 eV). Additional structures in which two CH_4 molecules are activated include $HIrCH_2(CH_3)^+(CH_4)$, $Ir(CH_3)_2^+(CH_4)$, and $(H)_2IrCH(CH_3)^+(CH_4)$. Finally, the activation of a single CH_4 molecule by Ir^+ is found in the $IrCH_2^+(CH_4)_2$ and $HIrCH^+(CH_4)_2$ structures. There were two structures for which triplet and/or quintet spin states were located, but a stable singlet intermediate was not found. The $Ir(CH_3)_2^+(CH_4)$ singlet species collapses to $HIr(CH_3)_3^+$ and the $Ir^+(CH_4)(C_2H_6)$ singlet structure could not be optimized.

The experimental depletion spectrum for $[^{193}Ir,3C\ 10H]^+$ is shown in Fig. 2a, where it is compared with B3LYP calculated spectra for select low-lying isomers. Fig. S5 shows comparisons to all isomers located. The experimental spectrum has prominent bands at 790, 1205, and 1355 cm^{-1} (the high-frequency scatter is considered as baseline, where experimental noise is amplified by the power correction). Three of the calculated spectra agree particularly well with the experimental spectrum: the singlet $HIr(CH_3)_3^+$, both trans and cis, and the triplet $Ir(CH_3)_2^+(CH_4)$ structure, which is much higher in energy (1.43 eV above the GS for B3LYP results). The $HIr(CH_3)_3^+$_trans structure, the B3LYP GS, has predicted bands at 792, 1206, 1343 cm^{-1}. These reproduce the three main bands observed in the experimental spectrum including their relative intensities. The spectrum for the $HIr(CH_3)_3^+$_cis species is similar to that of the $HIr(CH_3)_3^+$_trans spectrum except for the low energy band (815 cm^{-1}), which is clearly blue-shifted compared with experiment. The predicted spectrum of the lowest-lying triplet species, $Ir(CH_3)_2^+(CH_4)$, is also in reasonable agreement with the experimental spectrum, although the bands at 1186 and 1322 cm^{-1} do not agree with experiment as well as the $HIr(CH_3)_3^+$_trans GS. Two other low-energy structures, including the $(H)_2Ir(C_2H_4)^+(CH_4)$ MP2 GS, show significant differences with the observed spectrum, ruling out contributions from these species. On the basis of these comparisons, we assign the observed spectrum for [Ir,3C,10H]$^+$ to the $HIr(CH_3)_3^+$_trans GS. As pointed out by a reviewer, the observation of methane loss from this structure implies that sufficient IR excitation occurs before the molecule undergoes the rearrangement needed for this dissociation. The pathway for the needed rearrangement (the reverse of that needed to form the molecule in the first place) is outlined below.

4.2. Spectrum and Structures of [Ir,3C,8H]$^+$

Growth in the *m/z* 219 channel is attributed to loss of CH_4 from [^{191}Ir,3C,8H]$^+$, a product resulting from the elimination of two H_2 molecules upon activating three methane molecules. The depletion spectrum associated with the *m/z* 235 precursor is not useful for comparison because there are signs of both depletion and growth modes, Fig. S2. The relative energies for 27 unique geometries and spin states in 10 structural motifs for [Ir,3C,8H]$^+$ can be found in Table S6. The most relevant are shown in Fig. 2b with B3LYP energies in Table 1. Here, the GS is the singlet $HIrCH_3(C_2H_4)^+$ species for both B3LYP and MP2 calculations. The next lowest energy structure is similar to the GS and involves rearrangement of the ethene group to an ethylidene, $HIrCH_3(CHCH_3)^+$ (0.09 eV above the GS).

The experimental spectrum of [^{191}Ir,3C,8H]$^+$ is shown along with select singlet state theoretical spectra (and their associated structures) in Fig. 2b. Fig. S6 shows comparisons to all isomers and spin states located, where none of the additional species agree better with experiment than any of those shown in Fig. 2b. Among these, the spectrum for $IrCH_2(CH_3)_2^+$ does the best job of reproducing the experimental spectrum (although the relative intensities are not predicted well).

This structure reproduces a key feature of this spectrum, the peak located at 965 cm^{-1}, which is absent from the [^{193}Ir,3C,10H]$^+$ spectra. For the $IrCH_2(CH_3)_2^+$ species, this is the out-of-plane wagging motion of the Ir$^+$-CH$_2$ moiety. The broad peak between 1200 and 1400 cm^{-1} could be evidence for population of a second structure (perhaps contributions from the $HIrCH_3(C_2H_4)^+$ or $Ir(CH_2)_2^+(CH_4)$ species); however, broadening of the 1210, 1340, and 1380 cm^{-1} group of peaks for $IrCH_2(CH_3)_2^+$ could also describe the broad feature. The other two species included in Fig. 2b, $HIrCH_3(CHCH_3)^+$ and $HIrCH_2(C_2H_5)^+$, have peaks that are inconsistent with the observed spectrum and hence do not appear to contribute. Here too, the loss of methane from the $IrCH_2(CH_3)_2^+$ structure implies that sufficient IR excitation occurs before the molecule undergoes the rearrangement needed for this dissociation. Again, the pathway for the needed rearrangement (the reverse of that needed to form the molecule in the first place) is outlined below.

4.3. Reaction Coordinate Pathways for the Reaction of Ir$^+$ with 2 CH$_4$

In order to investigate the formation of the products assigned to the [Ir,3C,10H]$^+$ and [Ir,3C,8H]$^+$, we have examined the sequential reactions of x CH$_4$ molecules with Ir$^+$. The initial Ir$^+$ (^{5}F) + CH$_4$ reaction may yield both the HIrCH$^+$ (^{1}A′) + H$_2$ and IrCH$_2^+$ (^{3}A$_2$) + H$_2$ products, as previously demonstrated spectroscopically by Lapoutre *et al.* [13] No evidence for the higher energy alternate spin states, HIrCH$^+$ (^{3}A′) or IrCH$_2^+$ (^{1}A$_1$), was observed in that work. Nevertheless, pathways starting from both singlet and triplet forms of the Ir-carbene and Ir-carbyne hydride cation species were explored with relative B3LYP energies listed in Table 2 (both B3LYP and MP2 energies are listed in Table S7 of the Supporting Information).

The B3LYP RCPs of HIrCH$^+$ (^{1}A′,^{3}A′) reacting with CH$_4$ can be found in Fig. 3 with structures shown in Fig. 4 (singlet). Structures of the triplet species can be found in Fig. S7. Both reactions start by forming a HIrCH$^+$(CH$_4$) intermediate, ^{1}INT**1** and ^{3}INT**1**. On the singlet surface, ^{1}INT**1** has two pathways available that allow for $HIrCH_2(CH_3)^+$ (^{1}INT**3**) formation. The lowest energy pathway activates a C-H bond of methane via ^{1}TS1/2 to form the $(H)_2IrCH(CH_3)^+$ species, ^{1}INT**2**. Subsequent transfer of a hydrogen atom from Ir to the CH ligand via ^{1}TS2/3 forms ^{1}INT**3**, which lies 2.40 eV lower in energy than the Ir^+ + 2 CH_4 starting reactants. Alternatively, ^{1}INT**1** can transform directly to ^{1}INT**3** via ^{1}TS1/3, in which a CH bond of methane adds across the Ir-CH bond. This barrier is 0.06eV lower in energy than the starting reactants, but ~0.9 eV above ^{1}TS1/2. Note that B3LYP results put ^{1}INT**3** 0.65 eV below ^{1}INT**1**, whereas MP2 results predict the opposite, with ^{1}INT**1** favored by 0.28 eV. Further rearrangement of ^{1}INT**3** can occur to form the Ir-dimethyl species, ^{1}INT**4**, through ^{1}TS3/4 corresponding to transfer of the H atom from the Ir to the carbene. The ^{1}INT**4** intermediate is higher in energy than ^{1}INT3 (0.73eV) and therefore less likely to be formed. Fig. 3 also shows that ^{1}INT**3** can be formed directly by CH bond activation of methane by the $IrCH_2^+$ ($^1A'$) species, a process that is barrierless because Ir has an empty orbital that can accept electron density from the CH bond. This process is unlikely to be important in our experiment as formation of the $IrCH_2^+$ ($^1A_1$) reactant is endothermic with respect to the Ir^+ + CH_4 ground state precursors.

Dehydrogenation pathways that lead to the formation of $IrCH(CH_3)^+$ and $Ir(CH_2)_2^+$ products were also investigated. The former product can be formed from ^{1}INT**2** by forming a H-H bond in ^{1}TS2/5, which leads to $(H_2)IrCH(CH_3)^+$, ^{1}INT**5**. Removal of the bound H_2 molecule occurs via a loose transition state and requires 0.62 eV of energy from ^{1}INT**5**, overall a reaction that is exothermic by 0.66 eV. Formation of the $Ir(CH_2)_2^+$ product involves the transfer of a methyl hydrogen atom from ^{1}INT**3** through ^{1}TS3/6 and forms $(H)_2Ir(CH_2)_2^+$, ^{1}INT**6**. Formation of a H-H bond from ^{1}INT**6** occurs via ^{1}TS6/7 and leads to $(H_2)Ir(CH_2)_2^+$, ^{1}INT**7**. Again, removal of the H_2 molecule occurs through a loose transition state that is 0.30 eV higher in energy, but with an overall exothermicity of 0.94 eV.

On the triplet surface, Fig. 3b, $IrCH_2^+$ ($^3A_2$) reacts with CH_4 to form the $IrCH_2^+(CH_4)$ adduct, ^{3}INT**8**. From ^{3}INT**8**, a pathway is available through ^{3}TS8/3 to form the triplet state of $HIrCH_2(CH_3)^+$, ^{3}INT**3**. From here, a relatively low energy pathway exists for hydrogen atom transfer from Ir to CH_2 to form the triplet iridium dimethyl cation, $Ir(CH_3)_2^+$ ^{3}INT**4**, (about 2 eV below reactants at the B3LYP level, Table 2). ^{3}INT**4** is the lowest energy species along the triplet surface, but still lies 0.49 eV above ^{1}INT**3**. As noted above, no evidence for the formation of

$HIrCH^+$ ($^3A'$) was observed spectroscopically, such that its further reaction with methane is unlikely to be influential in the present study. Indeed, the surface shown in Fig. 3 shows that ^{3}TS1/2 is even higher in energy than this reactant, such that it would not activate another CH_4 even if it were formed.

Overall, the RCPs of Fig. 3 suggest that single dehydrogenation products from reaction of Ir^+ with two methanes are likely to be dominated by $HIrCH_2(CH_3)^+$ (^{1}INT**3**) and $Ir(CH_3)_2^+$ (^{3}INT**4**), where the latter species would be a minor contributor because its triplet precursor is a minor product. Double dehydrogenation products on the singlet surface are also energetically accessible and these pathways seem likely to form $Ir(CH_2)_2^+$ and $IrCH(CH_3)^+$.

4.4. Reaction Coordinate Pathways for the Reaction of Ir^+ with 3 CH_4

The singlet RCP for addition of a third methane to the iridium cation is shown in Fig. 5 with structures in Fig. 6. (Triplet surfaces and structures can be found in Figs. S8 and S9, respectively.) B3LYP relative energies are listed in Table 3 for both the singlet and triplet surfaces. Table S7 includes both B3LYP and MP2 relative single point energies for these species. These RCPs react methane with the likely products from Fig. 3, identified above. Along the singlet surface, CH_4 coordinates with $HIrCH_2(CH_3)^+$ (^{1}INT**3)** and forms ^{1}INT**9**, $HIrCH_2(CH_3)^+(CH_4)$, which has an energy of -2.77 eV relative to Ir^+ + 3 CH_4 reactants. From here, there are two pathways leading to formation of $HIr(CH_3)_3^+$_trans, ^{1}INT**11a**. The transfer of a H atom from the CH_4 ligand to the Ir atom occurs through ^{1}TS9/10 and leads to a shallow well associated with ^{1}INT**10**, $(H)_2IrCH_2(CH_3)_2^+$, which is only 0.02 eV lower than ^{1}TS9/10. A second hydrogen transfer from the Ir to the carbene occurs by ^{1}TS10/11 and is higher in energy than ^{1}INT**10** by 0.29 eV. The alternative pathway involves the direct hydrogen atom transfer from the CH_4 group to the carbene via ^{1}TS9/11. These pathways are energetically competitive with rate limiting steps differing by only 0.01 eV. Notably, ^{1}INT**11a** is the lowest energy species on both the singlet and triplet surfaces, consistent with its spectroscopic identification as the $[Ir,3C,10H]^+$ species. Furthermore, Fig. 5 shows that ^{1}INT**11a** formation from Ir^+ (^5F) + 3 CH_4 reactants is exothermic (by 3.68 eV) with no barriers in excess of the reactants. Finally, the reverse of the last CH_4 addition is also the mechanism for dissociation observed upon IR irradiation from this species yielding *m/z* 223, $[Ir, 2C, 8H]^+$.

Two competitive pathways are observed for the formation of the doubly dehydrogenated $IrCH_2(CH_3)_2^+$ species. The lower energy pathway starts with ^{1}INT**11a** and proceeds through ^{1}TS11/12 to form ^{1}INT**12**, $(H_2)IrCH_2(CH_3)_2^+$. This occurs through H-H bond formation between the metal-hydride and a hydrogen atom from one of the three methyl groups. Alternatively, ^{1}INT**12** can be formed directly from ^{1}INT**10** via ^{1}TS10/12, but this TS is only 0.13 eV higher in energy than ^{1}TS10/11, which is rate limiting for the aforementioned pathway. ^{1}INT**12** can lose H_2 through a loose transition state to form the $IrCH_2(CH_3)_2^+ + H_2$ products. This asymptote lies 0.13 eV higher in energy than ^{1}INT**12**, but the reaction is still exothermic from the initial $Ir^+ + 3\ CH_4$ reactants by 2.15 eV. Thus, formation of $IrCH_2(CH_3)_2^+ + 2\ H_2$ is consistent with spectroscopic identification of the ionic product as the $[Ir,3C,8H]^+$ species. Again Figure 5 shows that the decomposition pathway upon IR irradiation for this ion yielding *m/z* 219, $[Ir, 2C, 4H]^+$, is the reverse of the final CH_4 addition.

RCPs starting from the doubly dehydrogenated $Ir(CH_2)_2^+$ ($^1A_1$) and $IrCH(CH_3)^+$ ($^1A'$) products to form $IrCH_2(CH_3)_2^+$ are also considered in Table 3 and Fig. 5 with structures shown in Fig. 7. The $Ir(CH_2)_2^+$ species reacts through initial complexation with CH_4 to form $Ir(CH_2)_2^+(CH_4)$, ^{1}INT**13**, which is 1.36 eV lower in energy than the initial $Ir^+ + 3\ CH_4$ reactants. TS13/14 involves the transfer of a methane H atom to the Ir atom, is 0.56 eV higher in energy than ^{1}INT**13**, and forms ^{1}INT**14**, $HIr(CH_2)_2(CH_3)^+$. This intermediate can then transfer the H from the Ir atom to one carbene ligand over ^{1}TS14 forming the $IrCH_2(CH_3)_2^+$ intermediate. Alternatively, $IrCH(CH_3)^+$ reacts with methane to form $IrCH(CH_3)^+(CH_4)$, ^{1}INT**15**, which is 0.04 eV higher in energy than ^{1}INT**13** for B3LYP and lower by 0.67 eV for MP2. Transferring an H atom from the bound CH_4 molecule forms $HIrCH(CH_3)_2^+$, ^{1}INT**16**, over the barrier of TS15/16, 0.61 eV higher than ^{1}INT**15**. Final formation of the $IrCH_2(CH_3)_2^+$ intermediate involves transfer of the Ir-H atom to the carbyne group over ^{1}TS16, which has a barrier of 0.39 eV relative to ^{1}INT**16** for B3LYP (MP2 shows a barrierless transition to $IrCH_2(CH_3)_2^+$). These pathways may also contribute to the formation of the $[Ir,3C,8H]^+$ species observed experimentally, but are higher in energy than the $HIrCH_2(CH_3)^+$ + CH_4 pathway described above, as shown in Fig. 5.

On the triplet surface, shown in Fig. S8 with structures in Fig. S9, CH_4 attaches to $Ir(CH_3)_2^+$ ($^3B_1$), forming the $Ir(CH_3)_2^+(CH_4)$ species, ^{3}INT**17**. C-H bond activation through ^{3}TS17/11 forms $HIr(CH_3)_3^+$_trans, ^{3}INT**11**. This species is higher in energy than the triplet $Ir(CH_3)_2^+(CH_4)$ structure and lies well above its singlet analogue (^{1}INT**11a**), by 1.43 eV. Despite this, the triplet surface is energetically accessible from ground state Ir^+ + 3 CH_4. Thus, contributions to the $[Ir,3C,10H]^+$ experimental spectrum from the $Ir(CH_3)_2^+(CH_4)$ triplet structure cannot be ruled out, but are expected to be minor. Because of the higher relative energies associated with the triplet surface, their reactions with a fourth CH_4 molecule were not investigated further.

4.5. Spectrum and Structures of $[Ir,4C,12H]^+$

The heaviest 4C species examined here corresponds to the $[^{193}Ir,4C,12H]^+$ molecular formula, as measured by depletion of the *m/z* 253 channel. Formation of $[Ir,4C,12H]^+$ involves two dehydrogenations in the sequential reactions with four methane molecules. The 31 structures and spin states in 13 structural motifs located are listed with their relative 0 K energies in Table S9 (select values in Table 4) and are shown in Fig. S10. The singlet spin multiplicity is lowest in energy for all structures, except $Ir(CH_3)_2^+(C_2H_6)$ (no stable singlet geometry found) and $Ir(CH_2)_2^+(CH_4)_2$_trans (where the triplet is lower in energy for B3LYP). For all structures with singlet multiplicities, both B3LYP and MP2 calculations have the same energetic order (excluding the higher energy $IrCH_2(CH_3)_2^+(CH_4)_{CH2}$ structure). The $Ir(CH_3)_4^+$ structure is the GS and has four methyl groups bound in a tetrahedral arrangement around the Ir atom, Fig. 8a. The second lowest energy structure (0.27 eV above the GS for B3LYP) is $HIr(CH_3)_2(C_2H_5)^+$ and requires the formation of a C-C bond. The next lowest energy isomer, 0.53 eV above the GS, is the $HIr(CH_3)(C_2H_4)^+(CH_4)$ species, with $(H_2)Ir(CH_3)_2(C_2H_4)^+$ another 0.40 eV higher. In addition, there are three structures in which methane binds to $IrCH_2(CH_3)_2^+$. In the $IrCH_2(CH_3)_2^+(CH_4)_{Ir1}$

structure (1.11 eV), the methane ligand is bound to the open coordination site on Ir with a H_2C-Ir-CH_4 angle of 126º, Fig. 8a. The alternative $IrCH_2(CH_3)_2^+(CH_4)_{Ir2}$ structure (1.15 eV) again binds methane to Ir but the H_2C-Ir-CH_4 angle is now 160º. The $IrCH_2(CH_3)_2^+(CH_4)_{CH2}$ structure, shown in Fig. S10, has the methane ligand in a second coordination shell and has a relative energy greater than $IrCH_2(CH_3)_2^+(CH_4)_{Ir1}$ by 0.17 eV.

In Fig. 8a, the *m/z* 253 channel depletion spectrum is shown along with predicted spectra for select $[Ir,4C,12H]^+$ structures. Fig. S10 shows comparisons to all the isomers investigated in the current work. Although there is a favorable comparison between peaks in the experimental spectrum at 800, 1225, and 1375 cm^{-1} and those predicted for the $Ir(CH_3)_4^+$ GS at 820, 1215, and 1360 cm^{-1}, this symmetric species fails to reproduce peaks observed at 555, 740, 1030, 1165, and 1425 cm^{-1}. Rather, the experimental spectrum appears more satisfactorily explained by considering a combination of the spectra for the $HIr(CH_3)_2(C_2H_5)^+$ and $HIr(CH_3)(C_2H_4)^+(CH_4)$ species, the next two lowest energy isomers. The former species explains the intensity of the band at 1165 cm^{-1}, which is assigned to motions of the ethyl group. The latter species explains the peaks at 555 and 1030 cm^{-1}, which correspond to scissoring of the hydride and methyl groups and asymmetrical ethene CH_2 wagging motions, respectively. The next structure, $(H_2)Ir(CH_3)_2(C_2H_4)^+$ is also potentially consistent with the observed spectrum and cannot be eliminated on a spectroscopic basis. Likewise, contributions from any of the three $IrCH_2(CH_3)_2^+(CH_4)$ species cannot be ruled out. Although a definitive assignment of this spectrum is difficult, contributions from $HIr(CH_3)_2(C_2H_5)^+$ and $HIr(CH_3)(C_2H_4)^+(CH_4)$, which are coupled by C-H bond activation of the methane ligand, seem clear, but additional contributions from the $Ir(CH_3)_4^+$ GS and other low-lying structures are possible.

4.6. Spectrum and Structures of $[Ir,4C,10H]^+$

The spectra for depletion of *m/z* 249 and growth in the *m/z* 247 and 233 channels are all similar and therefore assigned to the $[^{191}Ir,4C,10H]^+$ molecular formula. This comparison suggests that the *m/z* 249 channel has two distinct dissociation pathways, H_2 loss forming *m/z* 247 and CH_4

loss forming *m/z* 233. Formation of $[Ir,4C,10H]^+$ requires dehydrogenation of three of the four reactant methane molecules. A total of 41 unique geometries and spin states with 15 structural motifs for this species were examined. Their relative energies can be found in Table S9 (with select values in Table 4) and Fig. S11 shows each structure adjacent to their respective predicted IR spectrum. In all cases where a stable singlet structure was found, the singlet spin multiplicity was lowest in energy. The six lowest energy structures found (all singlets) require formation of a C-C bond, most in the form of ethene C_2H_4, once as C_2H_5, and once as C_2H_3, Table S9. The lowest energy isomer found where no C-C coupling occurs is found at 1.11 eV above the GS. Formation of the $Ir(CH_3)_2(C_2H_4)^+$_C_s GS requires activation of all four methane molecules and the formation of a C–C bond. Here the ethene and two methyl ligands form a pyramidal structure around Ir, giving it C_s symmetry, Fig. 8b. At higher energies, singlet (0.24 eV), triplet (1.03 eV), and quintet (2.99 eV) spin states of C_{2v} isomeric forms of $Ir(CH_3)_2(C_2H_4)^+$ are found in which the ethene ligand is perpendicular to the H_3C-Ir-CH_3 plane. Calculations for the triplet and quintet $Ir(CH_3)_2(C_2H_4)^+$_C_s structures were found to converge to the $Ir(CH_3)_2(C_2H_4)^+$_C_{2v} species. The next lowest energy structure is the singlet $HIrCH_2(CH_3)(C_2H_4)^+$ species (0.47 eV above the GS). The $Ir(CH_2)_2(CH_3)_2^+$ singlet structure (1.11 eV above the GS) is the lowest energy structure that does not require the formation of a C–C bond. Four other singlet structures also do not require formation of a C–C bond: $IrCH(CH_3)_3^+$, $Ir(CH_2)_3^+(CH_4)$, $IrCH(CH_2)(CH_3)^+(CH_4)$, and $Ir(CH)_2^+(CH_4)_2$. These structures have relative energies ranging from 1.89 – 3.38 eV for B3LYP and 1.37 – 2.15 eV for MP2.

Fig. 8b compares the growth spectrum of *m/z* 233 with select vibrational spectra of various $[Ir,4C,10H]^+$ structures. This spectrum was chosen because CH_4 loss from the $[Ir,4C,10H]^+$ species is the dominant dissociation pathway. Fig. S11 compares this experimental spectrum with all the theoretical spectra investigated for the $[Ir,4C,10H]^+$ species. This experimental spectrum is best reproduced by the $Ir(CH_3)_2(C_2H_4)^+$_C_s GS, which replicates all the key spectral features well. For the $Ir(CH_3)_2(C_2H_4)^+$_C_s structure, there is a doublet of peaks at 1010 and 1035 cm^{-1}, which represents the symmetric and asymmetric ethene CH_2 wagging vibrations, respectively, which are blue shifted from the 943 and 949 cm^{-1} frequencies in free ethene, indicating ethene is partially activated [38]. The calculated spectrum of the $Ir(CH_3)_2(C_2H_4)^+$_C_{2v} species is very similar but shows only a single vibration near 1015 cm^{-1}, the asymmetric wag of the ethene H atoms. Because of the similarity of the two isomeric forms of $Ir(CH_3)_2^+(C_2H_4)$, only the GS spectrum is shown in Figure 8.

Fig. 8b also shows two additional low energy structures with a bound C_2H_4 group: $HIrCH_2(CH_3)(C_2H_4)^+$ and $IrCH_2(C_2H_4)^+(CH_4)$. These structures do a worse job of replicating the experimental spectrum and can be readily eliminated. In particular, these higher-energy isomers do not reproduce the band at 1015 cm^{-1} because their ethene wagging vibrations are closer to the free ethene frequencies, pointing to a less strongly bound ethene. The $Ir(CH_3)(C_2H_3)^+(CH_4)$ structure also has predicted peaks that are clearly absent in the experimental spectrum. The last structure shown in Fig. 8b is $Ir(CH_2)_2(CH_3)_2^+$, which has strong vibrational bands at around 875 and 1090 cm^{-1} that are absent from the experimental spectrum. Another spectrum of interest is that for $IrCH(CH_2)(CH_3)^+(CH_4)$ (2.77 eV above the GS), Fig. S11(l) of the Supporting Information. Population of this species would readily lead to CH_4 loss upon irradiation while also accounting for the 1015 cm^{-1} band (Ir-CH_2 and IrCH bends coupled symmetrically). Its spectrum matches experiment reasonably, but the predicted relative intensities are a poor match and the band predicted at 683 cm^{-1} is not experimentally observed. Furthermore, on an energetic basis, this species seems unlikely as it lies 0.47 eV above the $Ir^+(^5F)$ + 4 CH_4 reactants at the B3LYP level, although 1.70 eV below for MP2. Overall, we conclude that the $Ir(CH_3)_2(C_2H_4)^+$_C_s GS is the source of the growth spectrum.

For structures containing intact ethene, it would be intuitive to expect its loss upon IR excitation, resulting in growth in the *m/z* 221 channel; however, the distinct peak at 1015 cm^{-1} is not reproduced in the *m/z* 221 growth spectrum, indicating that this is not a dissociation channel. This strongly suggests that some rearrangement must occur from the theoretically predicted GS, resulting in the observed loss of either CH_4 or H_2, which will be discussed below. Again this implies that absorption of sufficient IR photons to induce dissociation occurs before these rearrangements.

4.7. Reaction Coordinate Pathways for the Reaction of Ir^+ with 4 CH_4

Formation of the assigned $[Ir,4C,12H]^+$ and $[Ir,4C,10H]^+$ products requires reaction with four CH_4 molecules. This process has been investigated through addition to both the singlet $HIr(CH_3)_3^+$_trans (^{1}INT**11a**) and $IrCH_2(CH_3)_2^+$ (^{1}INT**12**) species, identified as the $[Ir,3C,10H]^+$ and $[Ir,3C,8H]^+$ products above. B3LYP relative energies for these reaction pathways can be found in Table 5 (both B3LYP and MP2 values are in Table S10 of the Supporting Information) with the RCPs seen in Fig. 9 and structures shown in Fig. 10.

Complexation of CH_4 at multiple sites of the $IrCH_2(CH_3)_2^+$ species leads to the $IrCH_2(CH_3)_2^+(CH_4)_{Ir1}$ (^{1}INT**18a**), $IrCH_2(CH_3)_2^+(CH_4)_{Ir2}$ (^{1}INT**18b**), and $IrCH_2(CH_3)_2^+(CH_4)_{CH2}$ (^{1}INT**18c**) structures. From ^{1}INT**18b**, a CH bond of the methane adds across the Ir=CH_2 double bond in ^{1}TS18b/19, which leads directly to formation of $Ir(CH_3)_4^+$, ^{1}INT**19**, 3.45 eV below the Ir^+ + 4 CH_4 reactants. Alternatively, ^{1}INT**19** may be formed after rearrangement of ^{1}INT**11a** ($HIr(CH_3)_3^+$_trans) into ^{1}INT**11b** ($HIr(CH_3)_3^+$_cis), through ^{1}TS11 with a barrier of 0.28 eV and a reverse barrier of -0.01 eV (0.01 eV before zero point corrections). (Note that the spontaneous collapse of the cis isomer to trans predicted by B3LYP is consistent with observation of the latter spectroscopically, see above.) After this rearrangement, complexation of CH_4 to ^{1}INT**11b** forms the $HIr(CH_3)_3^+$_cis(CH_4) structure, ^{1}INT**23** (-3.53 eV). ^{1}INT**23** can then synchronously form a new H-H bond along with a new Ir-methyl bond through ^{1}TS23/24, which has a barrier of 1.80 eV. This forms ^{1}INT**24**, $(H_2)Ir(CH_3)_4^+$, which can lose H_2 through a loose transition state to produce $Ir(CH_3)_4^+$ (^{1}INT**19**). This tetramethyl structure is the lowest energy structure for both B3LYP and MP2, Tables 4 and S11. On this basis, the experimental presence of $Ir(CH_3)_4^+$ seems likely, even though other species are also clearly contributing.

Figs. 9 and 10 also show formation of the other structures in Fig. 8a as well as its dehydrogenation product, $Ir(CH_3)_2(C_2H_4)^+$, the $[Ir,4C,10H]^+$ product identified above. This process occurs from ^{1}INT**18c**. Here, the methane CH bond adds across the Ir=CH_2 π bond such that a new C–C bond is formed while transferring an H atom to the Ir center in ^{1}TS18c/20. This process forms $HIr(CH_3)_2(C_2H_5)^+$, ^{1}INT**20**. This intermediate can either lose H_2 or CH_4. Dehydrogenation can occur through the 5-membered ring ^{1}TS20/21, yielding $(H_2)Ir(CH_3)_2(C_2H_4)^+$, ^{1}INT**21**. Removal of the H_2 molecule forms $Ir(CH_3)_2(C_2H_4)^+$ + H_2 products, which lie 0.23 eV above ^{1}INT**21**. CH_4 loss can occur through the transfer of a terminal ethyl H atom to the nearest methyl group, ^{1}TS20/22, forming the $HIrCH_3(C_2H_4)^+(CH_4)$ intermediate, ^{1}INT**22**. Loss of CH_4 from ^{1}INT**22** takes 0.40 eV. Note that the pathways in Figure 9 show that formation of all of the five structures considered in Fig. 8a (along with ^{1}INT18b and ^{1}INT18c), as well as the [Ir,4C,10H]$^+$ GS, are energetically accessible with no barriers above the $Ir^+(^5F)$ + 4 CH_4 reactants.

4.8. Spectrum and Structures of [Ir,O,3C,12H]$^+$.

The *m/z* 257 and 255 channels correspond to the [Ir,O,3C,12H]$^+$ molecular formula, which is the prominent [Ir,3C,10H]$^+$ product noted above plus a water molecule. As discussed in detail in the Supporting Information, this species can be identified as the $HIr(CH_3)_3^+$ species with a water ligand bound to the iridium. Interestingly, the spectrum, shown in Figure S12, is most consistent with the cis isomer of this species, $HIr(CH_3)_3^+(H_2O)_{Ir}$_cis. This orientation of the methyl groups permits a stronger interaction of the water ligand with the Ir (an Ir-O bond distance of 2.36 Å compared with 2.44 Å in the trans conformer) as well as less steric interactions with the methyl groups. The observation of this species is consistent and strengthens the identification of the [Ir,3C,10H]$^+$ species as the trimethyl hydride iridium cation. B3LYP and MP2 relative energies for the species investigated can be found in Table S12.

5. Discussion of Experimental and Theoretical Results

The experimental results show that the sequential reaction of CH_4 with atomic Ir^+ leads to a number of products. As previously documented [6-9, 13], the initial reaction with a single methane involves efficient dehydrogenation, leading to a dominant product of $HIrCH^+$ ($^1A'$), with minor amounts of $IrCH_2^+$ ($^3A_2$). Under the present experimental conditions where excess methane is introduced, addition of a second methane leads to both single and double dehydrogenation products in comparable amounts. These processes are indicated in Fig. 3, which suggests that the dominant singlet species formed should be $HIrCH_2(CH_3)^+$ (single dehydrogenation) and $Ir(CH_2)_2^+$ (double dehydrogenation). Along the more minor and higher energy triplet pathway, the most likely product is $Ir(CH_3)_2^+$. Formation of this product parallels that observed in the reaction of Pt^+ with methane, where the $[Pt,2C,6H]^+$ product was spectroscopically identified as the dimethyl species [27]. Note that the triplet $Ir(CH_3)_2^+$ species will not readily dehydrogenate because this spin state cannot support the multiple bonds to Ir that make this energetically favorable for the singlet state.

Experimentally, addition of a third methane does not lead to further dehydrogenation and the single and double dehydrogenation products continue to have similar intensities. The associated RCPs are shown in Figure 5, which shows that the likely product formed by addition of methane to $HIrCH_2(CH_3)^+$ is $HIr(CH_3)_3^+$_trans, consistent with the assignment of this species to the spectrum observed for $[Ir,3C,10H]^+$ (the depletion spectrum of the *m/z* 239 channel and the growth spectrum of the *m/z* 223 channel). Growth of the *m/z* 219 channel was attributed to CH_4 loss from $[^{191}Ir,3C,8H]^+$, and its spectrum can be attributed mainly to $IrCH_2(CH_3)_2^+$ with minor contributions from $Ir(CH_2)_2^+(CH_4)$ and $HIrCH_3(C_2H_4)^+$ unable to be ruled out. The former species can be formed by reaction of the $Ir(CH_2)_2^+$ species with CH_4, as shown in Fig. 5, a pathway that can also form the minor contributor, $Ir(CH_2)_2^+(CH_4)$. $IrCH_2(CH_3)_2^+$ could also be plausibly generated by dehydrogenation of the dominant $HIr(CH_3)_3^+$ product, Fig. 5; however, the observation that the ratio of single and double dehydrogenation remains relatively constant for the 2C and 3C products indicates that this dehydrogenation does not occur extensively. Formation of the $HIrCH_3(C_2H_4)^+$ minor contributor can proceed by interaction with a fourth CH_4 molecule along the surface shown in Fig. 9 and subsequent loss of CH_4. For the minor triplet species, reaction of $Ir(CH_3)_2^+$ with methane probably leads to the triplet $Ir(CH_3)_2^+(CH_4)$ species as shown in Fig. S8. As noted above, a small amount of this species cannot be ruled out spectroscopically.

The reaction with a fourth CH_4 molecule shifts the number of dehydrogenations such that now double and triple dehydrogenations are observed, with loss of 3 H_2 dominating by about a factor of two. (As stated above, there is evidence for a minute amount of the single dehydrogenated $[^{193}Ir,4C,14H]^+$ species, but its intensity is too small to interrogate in the current work.) These results show that the addition of a fourth CH_4 molecule to the 3C products readily leads to dehydrogenation.

The $[Ir,4C,12H]^+$ spectrum is poorly replicated when *only* considering the $Ir(CH_3)_4^+$ GS. As shown in Fig. 8a, a mixture of the $HIr(CH_3)_2(C_2H_5)^+$ and $HIr(CH_3)(C_2H_4)^+(CH_4)$ isomers is needed to reproduce the experimental results, although contributions from $Ir(CH_3)_4^+$ and $IrCH_2(CH_3)_2^+(CH_4)$ are also feasible (with the former seemingly likely given its low energy). Here, the RCPs of Fig. 9 indicate that reaction of CH_4 with the dominant $HIr(CH_3)_3^+$ product can lead to the $Ir(CH_3)_4^+$ product via an appreciable barrier at TS23/24, which still lies well below the energy of the reactants. Fig. 9 also shows $IrCH_2(CH_3)_2^+(CH_4)$, INT**18**, is easily formed by simple addition of methane to the $IrCH_2(CH_3)_2^+$ product. This species can undergo further rearrangement over TS18b/19 to form $Ir(CH_3)_4^+$. Alternatively, the $HIr(CH_3)_2(C_2H_5)^+$ product, ^{1}INT**20**, nearly as stable as the $Ir(CH_3)_4^+$ product, can also be formed from INT**18** by passing over TS18c/20. Further, ^{1}INT**20** can rearrange over TS20/22 to yield $HIr(CH_3)(C_2H_4)^+(CH_4)$, ^{1}INT**22**. Thus, energetically reasonable pathways exist to form all four $[Ir,4C,12H]^+$ isomers that are consistent with the experimental spectrum.

Fig. 9 also shows that ^{1}INT**20** can dehydrogenate to yield $Ir(CH_3)_2(C_2H_4)^+\_C_s$, the species assigned as the likely $[Ir,4C,10H]^+$ product on the basis of excellent agreement between the experimental and theoretical spectra for this species. This dehydrogenation has a transition state with a similar energy to that for CH_4 loss forming $HIrCH_3(C_2H_4)^+$, which could be a minor contributor to the $[Ir,3C,8H]^+$ spectrum, as noted above.

We also considered the likely decomposition modes of the $Ir(CH_3)_2(C_2H_4)^+\_C_s$ structure. Although loss of C_2H_4 seems like a plausible pathway, there is no overlap between the depletion of the *m/z* 249 channel and growth in the *m/z* 221 channel that would suggest loss of C_2H_4. Instead, dissociation of $Ir(CH_3)_2(C_2H_4)^+$_C_s must involve rearrangement of the Ir-methyl groups such that CH_4 may be lost under IRMPD conditions. The various possible fragmentation pathways were investigated with the B3LYP potential energy surface shown in Fig. S13 and both B3LYP and MP2 energies are listed in Table S13. These results indicate that loss of C_2H_4 is a higher energy process than dehydrogenation by 0.89 eV and CH_4 loss pathways by 0.71 eV, consistent with the experimentally observed pathways. A similar rearrangement and loss of CH_4 was previously observed in the IRMPD study of $Pt(CH_3)_2^+$ [27].

6. Conclusion

The present results illustrate methane activation and dehydrogenation in the sequential reactions of CH_4 with gas-phase atomic Ir^+. By comparing experimental spectra with theoretical results, we are able to consider the structural composition and mechanistic pathways for the formation of a number of the experimentally observed product channels. Assignment of the $[^{193}Ir,3C,10H]^+$ and $[^{191}Ir,4C,10H]^+$ spectra, from depletion of the *m/z* 239 channel and growth in the *m/z* 233 channels, are made with the most confidence and are attributed to the singlet $HIr(CH_3)_3^+$_trans (**11a**) and $Ir(CH_3)_2(C_2H_4)^+$_C_s species, respectively. Assignments of the $[^{191}Ir,3C,8H]^+$ and $[^{193}Ir,4C,12H]^+$ spectra were more complicated but likely assignments are $IrCH_2(CH_3)_2^+$ and a mixture of $HIr(CH_3)_2(C_2H_5)^+$ and $HIr(CH_3)(C_2H_4)^+(CH_4)$, along with $Ir(CH_3)_4^+$ and $(H_2)Ir(CH_3)_2(C_2H_4)^+$, respectively. Importantly, there is substantial evidence for C-C bond formation in the sequential reaction with four CH_4 molecules.

Supporting Information

Discussion of the growth and depletion spectra observed, along with the spectrum and structures of the $[Ir,O,3C,12H]^+$ species, is included. Table S1 lists B3LYP energies, symmetry, and zero-point energy along with MP2 energies for structures examined within the current work. Comparisons between experimental BDEs and both B3LYP and MP2 BDEs can be found for test systems in Table S2. Table S3 provides possible identities of all mass peaks observed and Table

S4 provides the pathways between these. Tables S5, S6, S9, S10, and S12 provide 0 K relative energies at both B3LYP and MP2 levels for all spin states of $[Ir,3C,10H]^+$, $[Ir,3C,8H]^+$, $[Ir,4C,12H]^+$, $[Ir,4C,10H]^+$, and $[Ir,O,3C,12H]^+$, respectively. Tables S7, S8, and S11 list both B3LYP and MP2 relative energies (with respect to the reactants) for Ir^+ + 2 CH_4, 3 CH_4, and 4 CH_4, respectively. Table S13 provides 0 K relative energies at both B3LYP and MP2 levels for several decomposition pathways of $Ir(CH_3)_2(C_2H_4)^+$. Figures S1 – S4 show depletion and growth spectra for all mass channels corresponding to $[Ir,2C,yH]^+$, $[Ir,3C,yH]^+$, $[Ir,4C,yH]^+$, and $[Ir,O,3C,yH]^+$, respectively. Figures S5, S6, S10, S11, and S12 show comparisons between experimental spectra for all spin states of all structures located for $[Ir,3C,10H]^+$, $[Ir,3C,8H]^+$, $[Ir,4C,12H]^+$, $[Ir,4C,10H]^+$, and $[Ir,O,3C,12H]^+$, respectively. Figures S7 shows structures of the triplet species in Figures 3. Figure S8 shows the triplet pathways for reaction of $Ir(CH_3)_2^+$ + CH_4 with structures shown in Figure S9. Figure S13 shows reaction coordinate pathways for decomposition of $Ir(CH_3)_2(C_2H_4)^+\_C_s$. Coordinates for all structures are available from the authors upon request.

Author Information.

Corresponding Author: *P.B.A.: e-mail, armentrout@chem.utah.edu.

Notes

The authors declare no competing financial interest.

Acknowledgement.

Financial assistance was provided by the National Science Foundation, Grants No. CHE-1664618 and OISE-1357887. We gratefully acknowledge the Nederlandse Organisatie voor Wetenschappelijk Onderzoek (NWO) for the support of the FELIX Laboratory. Finally, the Center for High Performance Computing (CHPC) at the University of Utah is acknowledged for their generous allocation of computing time.

References

[1] J.A. Labinger, J.E. Bercaw, Understanding and Exploiting C-H Bond Activation, Nature, 417 (2002) 507-514.

[2] H. Schwarz, Chemistry with Methane: Concepts Rather than Recipes, Angew. Chem. Int. Ed. , 50 (2011) 10096-10115.

[3] H. Schwarz, How and Why Do Cluster Size, Charge State, and Ligands Affect the Course of Metal-Mediated Gas-Phase Activation of Methane?, Isr. J. Chem., 54 (2014) 1413-1431.

[4] J. Roithová, D. Schröder, Selective Activation of Alkanes by Gas-Phase Metal Ions, Chem. Rev., 110 (2010) 1170–1211.

[5] P.B. Armentrout, Methane Activation by 5 d Transition Metals: Energetics, Mechanisms, and Periodic Trends, Chem. – Eur. J., 23 (2017) 10-18.

[6] K.K. Irikura, J.L. Beauchamp, Methane Oligomerization in the Gas Phase by Third-Row Transition-Metal Ions, J. Am. Chem. Soc., 113 (1991) 2769-2770.

[7] K.K. Irikura, J.L. Beauchamp, Electronic Structure Considerations for Methane Activation by Third-Row Transition-Metal Ions, J. Phys. Chem., 95 (1991) 8344-8351.

[8] F.-X. Li, X.-G. Zhang, P.B. Armentrout, The Most Reactive Third-row Transition Metal: Guided Ion Beam and Theoretical Studies of the Activation of Methane by Ir^+, Int. J. Mass Spectrom., 255/256 (2006) 279-300.

[9] A. Shayesteh, V.V. Lavrov, G.K. Koyanagi, D.K. Bohme, Reactions of Atomic Cations with Methane: Gas Phase Room-Temperature Kinetics and Periodicities in Reactivity, J. Phys. Chem. A, 113 (2009) 5602–5611.

[10] G. Gioumousis, D.P. Stevenson, Reactions of Gaseous Molecule Ions with Gaseous Molecules. V. Theory, J. Chem. Phys., 29 (1958) 294-299.

[11] P.B. Armentrout, L. Parke, C. Hinton, M. Citir, Activation of Methane by Os^+: Guided Ion Beam and Theoretical Studies, ChemPlusChem 78 (2013) 1157-1173.

[12] X.-G. Zhang, R. Liyanage, P.B. Armentrout, The Potential Energy Surface for Activation of Methane by Pt^+: A Detailed Guided-Ion Beam Study, J. Am. Chem. Soc., 123 (2001) 5563-5575.

[13] V.J.F. Lapoutre, B. Redlich, A.F.G. van der Meer, J. Oomens, J.M. Bakker, A. Sweeney, A. Mookherjee, P.B. Armentrout, Structures of the Dehydrogenation Products of Methane Activation by 5d Transition Metal Cations, J Phys Chem. A, 117 (2013) 4115-4126.

[14] J.M. Bakker, V.J.F. Lapoutre, B. Redlich, J. Oomens, B.G. Sartakov, A. Fielicke, G. von Helden, G. Meijer, A.F.G. van der Meer, Intensity-Resolved IR Multiple Photon Ionization and Fragmentation of C_{60}, J. Chem. Phys., 132 (2010) 074305.

[15] C.J. Owen, G.C. Boles, V. Chernyy, J.M. Bakker, P.B. Armentrout, Structures of the Dehydrogenation Products of Methane Activation by 5d Transition Metal Cations Revisited: Deuterium Labeling and Rotational Contours, J. Chem. Phys., 148 (2018) 044307.

[16] P.B. Armentrout, S.E.J. Kuijpers, O.V. Lushchikova, R.L. Hightower, G.C. Boles, J.M. Bakker, Spectroscopic Identification of the Carbyne Hydride Structure of the Dehydrogenation Product of Methane Activation by Osmium Cations, J. Am. Soc. Mass. Spectrom. 29 (2018) 1781-1790. DOI: 10.1007/s13361-018-1929-7.

[17] O. Rodriguez Jr, J.M. Lisy, Infrared Spectroscopy of $Li^+(CH_4)_n$, $n = 1–9$, Clusters, Chem. Phys. Lett., 502 (2011) 145-149.

[18] O. Rodriguez, J.M. Lisy, Infrared Spectroscopy of $Li^+(CH_4)_1Ar_n$, $n = 1−6$, Clusters, J. Phys. Chem. A, 115 (2011) 1228-1233.

[19] B.L.J. Poad, C.D. Thompson, E.J. Bieske, Infrared Spectra of Mass-Selected $Al^+–(CH_4)_n$ $n = 1–6$ Clusters, Chem. Phys., 346 (2008) 176-181.

[20] V. Dryza, E.J. Bieske, Infrared Spectra and Density Functional Theory Calculations for $Mn^+–(CH_4)_n$ (n = 1–6) Clusters, Int. J. Mass spectrom., 297 (2010) 46-54.
[21] M. Citir, G. Altinay, G. Austein-Miller, R.B. Metz, Vibrational Spectroscopy and Theory of $Fe^+(CH_4)_n$ (n = 1−4), J. Phys. Chem. A, 114 (2010) 11322-11329.
[22] M.A. Ashraf, C.W. Copeland, A. Kocak, A.R. McEnroe, R.B. Metz, Vibrational Spectroscopy and Theory of $Fe_2^+(CH_4)_n$ (n = 1-3), Phys. Chem. Chem. Phys., 17 (2015) 25700-25704.
[23] A. Kocak, Z. Sallese, M.D. Johnston, R.B. Metz, Vibrational Spectroscopy of $Co^+(CH_4)_n$ and $Ni^+(CH_4)_n$ (n = 1–4), J. Phys. Chem. A, 118 (2014) 3253-3265.
[24] A. Kocak, M.A. Ashraf, R.B. Metz, Vibrational Spectroscopy Reveals Varying Structural Motifs in $Cu^+(CH_4)_n$ and $Ag^+(CH_4)_n$ (n = 1–6), J. Phys. Chem. A, 119 (2015) 9653-9665.
[25] D.J. Harding, C. Kerpal, G. Meijer, A. Fielicke, Activated Methane on Small Cationic Platinum Clusters, Angew. Chem. Int. Ed., 51 (2012) 817-819.
[26] S.M. Lang, T.M. Bernhardt, V. Chernyy, J.M. Bakker, R.N. Barnett, U. Landman, Selective C-H Bond Cleavage in Methane by Small Gold Clusters, Angew. Chem. Int. Ed. Engl., 56 (2017) 13406-13410.
[27] O.W. Wheeler, M. Salem, A. Gao, J.M. Bakker, P.B. Armentrout, Activation of C–H Bonds in $Pt^+ + x\, CH_4$ Reactions, where x = 1–4: Identification of the Platinum Dimethyl Cation, J. Phys. Chem. A, 120 (2016) 6216-6227.
[28] D.M. Kiawi, J.M. Bakker, J. Oomens, W.J. Buma, Z. Jamshidi, L. Visscher, L.B.F.M. Waters, Water Adsorption on Free Cobalt Cluster Cations, J. Phys. Chem. A, 119 (2015) 10828-10837.
[29] D. Oepts, A.F.G. van der Meer, P.W. van Amersfoort, The Free-Electron-Laser User Facility FELIX, Infrared Phys. Technol., 36 (1995) 297-308.
[30] J.M. Bakker, Structural Identification of Gas-Phase Biomolecules Using Infrared Spectroscopy, in, Radboud University Nijmegen, 2004.
[31] M.J. Frisch, G.W. Trucks, H.B. Schlegel, G.E. Scuseria, M.A. Robb, J.R. Cheeseman, G. Scalmani, V. Barone, B. Mennucci, G.A. Petersson, H. Nakatsuji, M. Caricato, X. Li, H.P. Hratchian, A.F. Izmaylov, J. Bloino, G. Zheng, J.L. Sonnenberg, M. Hada, M. Ehara, K. Toyota, R. Fukuda, J. Hasegawa, M. Ishida, T. Nakajima, Y. Honda, O. Kitao, H. Nakai, T. Vreven, J.A. Montgomery, J.E. Peralta, F. Ogliaro, M. Bearpark, J.J. Heyd, E. Brothers, K.N. Kudin, V.N. Staroverov, R. Kobayashi, J. Normand, K. Raghavachari, A. Rendell, J.C. Burant, J.M. Millam, S.S. Iyengar, J. Tomasi, M. Cossi, N. Rega, J.M. Millam, M. Klene, J.E. Knox, J.B. Cross, V. Bakken, C. Adamo, J. Jaramillo, R. Gomperts, R.E. Stratmann, O. Yazyev, A.J. Austin, R. Cammi, C. Pomelli, J.W. Ochterski, R.L. Martin, K. Morokuma, V.G. Zakrzewski, G.A. Voth, P. Salvador, J.J. Dannenberg, S. Dapprich, A.D. Daniels, O. Farkas, J.B. Foresman, J.V. Ortiz, J. Cioslowski, D.J. Fox, Gaussian 09, Revision A.02, in, Gaussian Inc., Pittsburgh, PA, 2009.
[32] C. Lee, W. Yang, R.G. Parr, Development of the Colle-Salvetti Correlation-Energy Formula into a Functional of the Electron Density, Phys. Rev. B, 37 (1988) 785-789.
[33] A.D. Becke, Density-Functional Thermochemistry. III. The Role of Exact Exchange, J. Chem. Phys., 98 (1993) 5648-5652.
[34] F. Weigend, R. Ahlrichs, Def2-SVP Basis Sets, Phys. Chem. Chem. Phys., 7 (2005) 3297-3305.
[35] M.K. Kesharwani, B. Brauer, J.M.L. Martin, Frequency and Zero-Point Vibrational Energy Scale Factors for Double-Hybrid Density Functionals (and Other Selected Methods): Can Anharmonic Force Fields Be Avoided?, J. Phys. Chem. A, 119 (2015) 1701-1714.

[36] B. Ruscic, D. Feller, K.A. Peterson, Active Thermochemical Tables: Dissociation Energies of Several Homonuclear First-Row Diatomics and Related Thermochemical Values, Theor. Chem. Acc., 133 (2013) 1415.
[37] T. Walczyk, K.G. Heumann, Iridium Isotope Ratio Measurements by Negative Thermal Ionization Mass Spectrometry and Atomic Weight of Iridium, Int. J. Mass Spectrom. Ion Processes, 123 (1993) 139-147.
[38] T. Shimanouchi, Tables of Molecular Vibrational Frequencies Consolidated, Volume I, NSRDS-NBS, 39 (1972) 1.

Table 1. Relative energies (eV) calculated for $[Ir,3C,10H]^+$ and $[Ir,3C,8H]^+$ structures at 0 K.[a]

Molecular Formula:	Spin = 1	3	5
$[Ir,3C,10H]^+$	B3LYP[b]	B3LYP[b]	B3LYP[b]
$HIr(CH_3)_3^+$_trans	0.00	2.05	–
$(H)_2Ir(C_2H_4)^+(CH_4)$	0.18	1.73	4.05
$HIr(CH_3)_3^+$_cis	0.29	2.15	4.12
$(H)_2Ir(CHCH_3)^+(CH_4)$	0.41	2.31	4.47
$HIrC_2H_5^+(CH_4)$	0.49	1.72	3.64
$HIrCH_2(CH_3)^+(CH_4)$	0.91	2.56	4.35
$Ir(CH_3)_2^+(CH_4)$	–	1.43	–
$[Ir,3C,8H]^+$			
$HIrCH_3(C_2H_4)^+$	0.00	0.99	–
$HIrCH_3(CHCH_3)^+$	0.09	1.47	3.55
$IrCH_2(CH_3)_2^+$	0.36	1.52	3.81
$HIrCH_2(C_2H_5)^+$	0.58	2.15	3.81
$Ir(CH_2)_2^+(CH_4)$	1.16	2.29	4.13

[a] Geometries optimized at the B3LYP/def2-TZVPPD level of theory. The – symbol indicates failure to find a stable intermediate for the designated structure and spin state. Values listed are for the lowest energy species found for a specific molecular formula. [b] B3LYP/def2-TZVPPD single point energies with zero-point energy corrections.

Table 2. Reaction coordinate pathways (in eV) for the $HIrCH^+ + CH_4$ and $IrCH_2^+ + CH_4$ reactions at 0 K.[a]

	Spin = 1	3
Species	B3LYP[b]	B3LYP[b]
$HIrCH^+ + CH_4$	-0.85	0.16
$HIrCH^+(CH_4)$ (**1**)	-1.75	-0.48
TS1/2	-0.94	0.62
TS1/3	-0.06	0.40
$(H)_2IrCH(CH_3)^+$ (**2**)	-1.16	-0.15
TS2/3	-1.00	0.16
TS2/5	-1.12	–
$HIrCH_2(CH_3)^+$ (**3**)	-2.40	-1.10
TS3/4	-1.32	-0.79
TS3/6	-1.36	–
$Ir(CH_3)_2^+$ (**4**)	-1.67	-1.91
$(H_2)IrCH(CH_3)^+$ (**5**)	-1.28	–
$IrCH(CH_3)^+ + H_2$	-0.66	–
$(H)_2Ir(CH_2)_2^+$ (**6**)	-1.60	–
TS6/7	-1.08	–
$(H_2)Ir(CH_2)_2^+$ (**7**)	-1.24	–
$Ir(CH_2)_2^+ + H_2$	-0.94	–
$IrCH_2^+ + CH_4$	0.04	-0.60
$IrCH_2^+(CH_4)$ (**8**)	–	-1.24
TS8/3	–	-0.62

[a] All energies shown relative to the $Ir^+ + 2\ CH_4$ reactants including the energy of an H_2 product (not shown) and are zero-point energy corrected. [b] B3LYP/def2-TZVPPD single point energies from B3LYP/def2-TZVPPD geometry optimized structures.

Table 3. Reaction coordinate pathways (in eV) for reaction of CH_4 with $HIrCH_2(CH_3)^+$, $Ir(CH_2)_2^+$, $IrCH(CH_3)^+$, and $Ir(CH_3)_2^+$ at 0 K.[a]

Species	Spin = 1		1
	B3LYP[b]		B3LYP[b]
$HIrCH_2(CH_3)^+$ (**3**) + CH_4	-2.40	$IrCH(CH_3)^+$ + CH_4 + H_2	-0.66
$HIrCH_2(CH_3)^+(CH_4)$ (**9**)	-2.77	$IrCH(CH_3)^+(CH_4)$ (**15**) + H_2	-1.32
TS9/10	-2.09	TS15/16 + H_2	-0.71
TS9/11	-1.81	$HIrCH(CH_3)_2^+$ (**16**) + H_2	-0.94
$(H)_2IrCH_2(CH_3)_2^+$ (**10**)	-2.11	TS16 + H_2	-0.55
TS10/11	-1.82		
TS10/12	-1.69		Spin = 3
$HIr(CH_3)_3^+$_trans (**11a**)	-3.68	Species	B3LYP[b]
TS11/12	-1.89	$Ir(CH_3)_2^+$ + CH_4	-1.91
$(H_2)IrCH_2(CH_3)_2^+$(**12**)	-2.28	$Ir(CH_3)_2^+(CH_4)$ (**17**)	-2.25
$IrCH_2(CH_3)_2^+$ + H_2	-2.15	TS17/11	-1.51
$Ir(CH_2)_2^+$ + CH_4 + H_2	-0.94	$HIr(CH_3)_3^+$_trans (**11**)	-1.63
$Ir(CH_2)_2^+(CH_4)$ (**13**) + H_2	-1.36		
TS13/14 + H_2	-0.80		
$HIr(CH_2)_2(CH_3)^+$ (**14**) + H_2	-0.91		
TS14 + H_2	-0.46		

[a] All energies shown are relative to Ir^+ (^5F) + 3 CH_4 reactants and therefore include the energy of H_2 product formed in the initial dehydrogenation reaction between Ir^+ and the first CH_4 molecule. All energies include zero-point energy corrections. [b] B3LYP/def2-TZVPPD single point energies.

Table 4. Relative energies (eV) calculated for $[Ir,4C,12H]^+$ and $[Ir,4C,10H]^+$ structures at 0 K.[a]

Molecular Formula	Spin = 1	3	5
$[Ir,4C,12H]^+$	B3LYP[b]	B3LYP[b]	B3LYP[b]
$Ir(CH_3)_4^+$	0.00	2.07	4.05
$HIr(CH_3)_2(C_2H_5)^+$	0.27	2.36	4.35
$HIr(CH_3)(C_2H_4)^+(CH_4)$	0.53	–	3.96
$(H_2)Ir(CH_3)_2(C_2H_4)^+$	0.93	2.51	4.09
$IrCH_2(CH_3)_2^+(CH_4)_{Ir1}$	1.11	–	4.50
$IrCH_2(CH_3)_2^+(CH_4)_{Ir2}$	1.15	–	–
$[Ir,4C,10H]^+$			
$Ir(CH_3)_2(C_2H_4)^+\_C_s$	0.00	–	–
$Ir(CH_3)_2(C_2H_4)^+\_C_{2v}$	0.24	1.03	2.99
$HIrCH_2(CH_3)(C_2H_4)^+$	0.47	1.90	4.18
$IrCH_2(C_2H_4)^+(CH_4)$	0.53	1.92	3.33
$IrCH_2(CH_3)(C_2H_5)^+$	0.64	1.77	3.97
$IrCH_3(C_2H_3)^+(CH_4)$	1.01	1.57	3.32
$Ir(CH_2)_2(CH_3)_2^+$	1.11	2.31	4.58

[a] Geometries optimized at the B3LYP/def2-TZVPPD level of theory. The – symbol indicates failure to find a stable intermediate for the designated structure and spin state. Values listed are for the lowest energy species found for a specific molecular formula. [b] B3LYP/def2-TZVPPD single point energies with zero-point energy corrections.

Table 5. Reaction coordinate pathways (in eV) for the singlet spin $IrCH_2(CH_3)_2^+$ + CH_4 reaction at 0 K.[a]

Species	B3LYP[b]	Species	B3LYP[b]
$IrCH_2(CH_3)_2^+ + CH_4$	-2.15	$HIr(CH_3)_3^+$_trans (**11a**) + CH_4	-3.68
$IrCH_2(CH_3)_2^+(CH_4)_{Ir1}$ (**18a**)	-2.34	TS11 + CH_4	-3.40
TS18a/18b	-2.30	$HIr(CH_3)_3^+$_cis (**11b**) + CH_4	-3.39
$IrCH_2(CH_3)_2^+(CH_4)_{Ir2}$ (**18b**)	-2.30	$HIr(CH_3)_3^+$_cis(CH_4) (**23**)	-3.53
TS18b/19	-1.20	TS23/24	-1.73
$Ir(CH_3)_4^+$ (**19**)	-3.45	$(H_2)Ir(CH_3)_4^+$ (**24**)	-3.45
$IrCH_2(CH_3)_2^+(CH_4)_{CH2}$ (**18c**)	-2.17		
TS18c/20	-1.06		
$HIr(CH_3)_2(C_2H_5)^+$ (**20**)	-3.19		
TS20/21	-1.67		
$(H_2)Ir(CH_3)_2(C_2H_4)^+$ (**21**)	-2.53		
$Ir(CH_3)_2(C_2H_4)^+$_C_s + H_2	-2.30		
TS20/22	-1.65		
$HIr(CH_3)(C_2H_4)^+(CH_4)$ (**22**)	-2.92		
$HIr(CH_3)(C_2H_4)^+$ + (CH_4)	-2.52		

[a] All energies shown relative to Ir^+ (^5F) + 4 CH_4 reactants and include either H_2 or 2 H_2 energies and zero-point energy corrections. [b] B3LYP/def2-TZVPPD single point energies.

Figure Captions

Fig. 1. Mass scans of the $Ir^+ + x\ CH_4$ reaction system both with (red, offset by -0.5 amu) and without (black) irradiation by FELIX at 1015 cm^{-1}. The ticks on the bottom axis are labeled by the maximum number of H atoms that can be found for the corresponding $x\ CH_4$ system. Data for *m/z* 191 – 211, 226 – 232, 240 – 247, and 254 – 259 have been multiplied by 30 and offset by 0.1 above the original data for both red and black.

Fig. 2. Scaled IRMPD *m/z* 239 depletion yield spectrum for $[^{193}Ir,3C,10H]^+$ (in shade, a) and *m/z* 219 growth yield spectrum for $[^{191}Ir,3C,8H]^+$ (in shade, b) with calculated singlet (unless otherwise specified) B3LYP/def2-TZVPPD spectra for select isomers of interest. Relative energies in eV are displayed at the B3LYP levels including zero point energies. Optimized structures are found to the right of the corresponding spectrum.

Fig. 3. Reaction coordinate pathways for the singlet (red) and triplet (blue) surfaces of the $HIrCH^+ + CH_4$ and $IrCH_2^+ + CH_4$ reactions are shown. Geometry optimizations and single point energy calculations were performed at the B3LYP/def2-TZVPPD level of theory and include zero-point energy corrections. Each step in color includes energy for the H_2 product lost in the initial dehydrogenation process, which is shown by thick dashed lines as taken from Ref. [13]. Formation of the singlet $IrCH_2^+$ and triplet $HIrCH^+$ species have rate-limiting transition states abbreviated LTS.

Fig. 4. B3LYP/def2-TZVPPD geometry optimized structures for the singlet reaction pathways shown in Figure 3. Energies in eV relative to $Ir^+(^5F) + 2\ CH_4$ are displayed at the B3LYP levels including zero point energies.

Fig. 5. Reaction coordinate pathways for the singlet $HIrCH_2(CH_3)^+ + CH_4$ (red) and $Ir(CH_2)_2^+/IrCH(CH_3)^+ + CH_4$ (purple) surfaces are shown. Geometry optimizations performed at

the B3LYP/def2-TZVPPD level of theory and single point energies include the zero-point energy corrections from optimized structures. All energies are relative to the Ir^+ (^5F) + 3 CH_4 reactants and include the energy of the H_2 product(s) formed in the initial dehydrogenation process(es).

Fig. 6. B3LYP/def2-TZVPPD geometry optimized structures for the singlet $HIrCH_2(CH_3)^+$ + CH_4 reaction pathways shown in Figure 5. Energies in eV relative to $Ir^+(^5F)$ + 3 CH_4 are displayed at the B3LYP levels including zero point energies.

Fig. 7. B3LYP/def2-TZVPPD geometry optimized structures for the singlet $Ir(CH_2)_2^+$ + CH_4 and $IrCH(CH_2)^+$ + CH_4 reaction pathways shown in Figure 5. Energies in eV relative to $Ir^+(^5F)$ + 3 CH_4 are displayed at the B3LYP levels including zero point energies.

Fig. 8. Scaled IRMPD *m/z* 253 depletion yield spectrum for $[^{193}Ir,4C,12H]^+$ (in shade, a) and *m/z* 233 growth yield spectrum for $[^{191}Ir,4C,10H]^+$ (in shade, b) with calculated B3LYP/def2-TZVPPD spectra for select isomers. Relative energies in eV are displayed at the B3LYP levels including zero point energies. The corresponding structures are shown to the right of their respective spectrum.

Fig. 9. Reaction coordinate pathways for $IrCH_2(CH_3)_2^+$ and $HIr(CH_3)_3^+$_trans + CH_4 with single point energies from B3LYP/def2-TZVPPD geometry optimizations and zero-point energy corrected. All energies are relative to the Ir^+ (^5F) + 4 CH_4 reactants and include the energy of the H_2 product(s) formed in the initial dehydrogenation process(es).

Fig. 10. B3LYP/def2-TZVPPD geometry optimized structures for the singlet reaction pathways shown in Figure 9. Energies in eV relative to $Ir^+(^5F)$ + 4 CH_4 are displayed at the B3LYP levels including zero point energies.

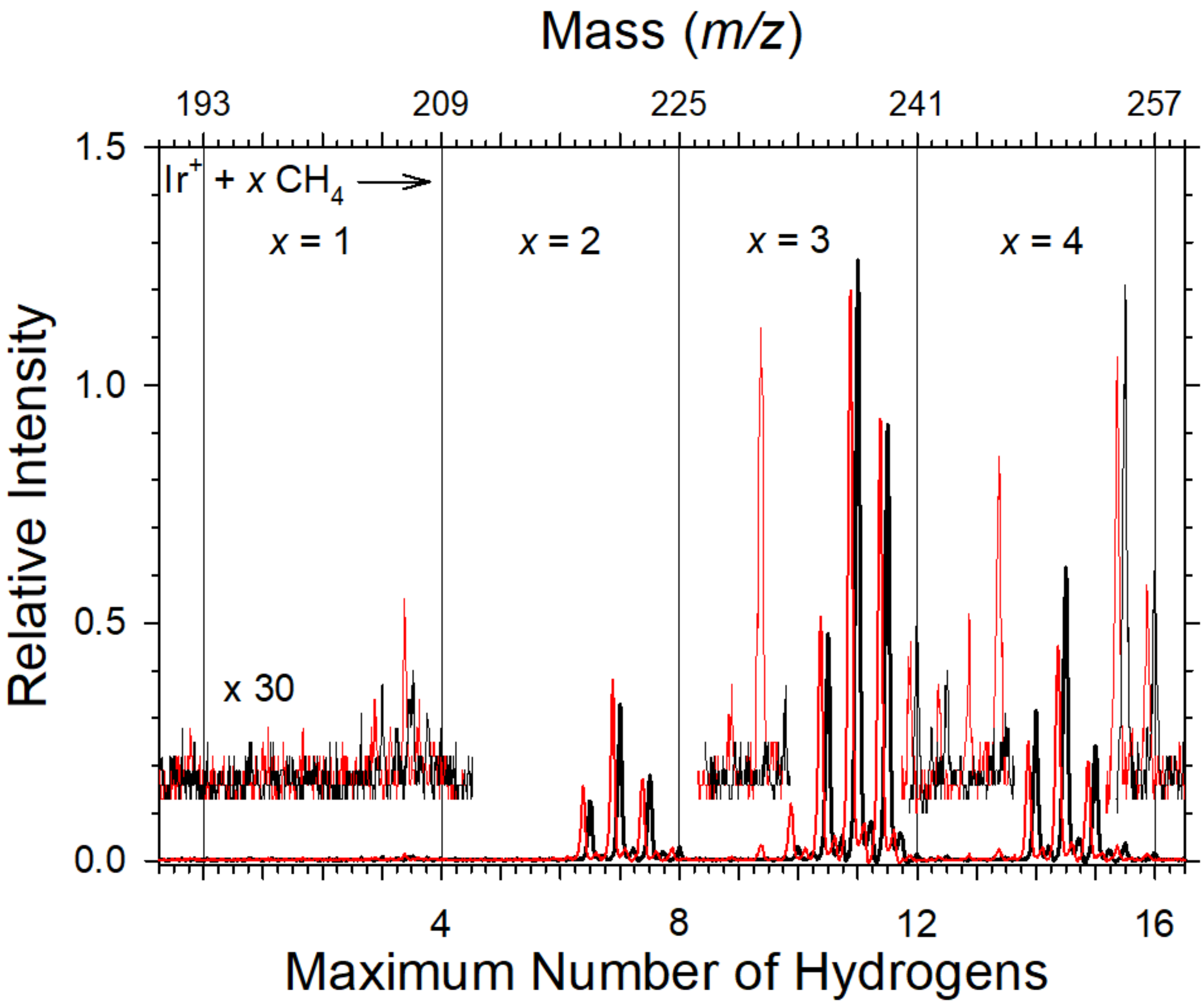
Mass (m/z)
193
209
225
241
257
1.5
1.0
0.5
0.0
Relative Intensity
$Ir^+ + x\, CH_4 \longrightarrow$
$x = 1$
$x = 2$
$x = 3$
$x = 4$
x 30
4
8
12
16
Maximum Number of Hydrogens

Figure 1

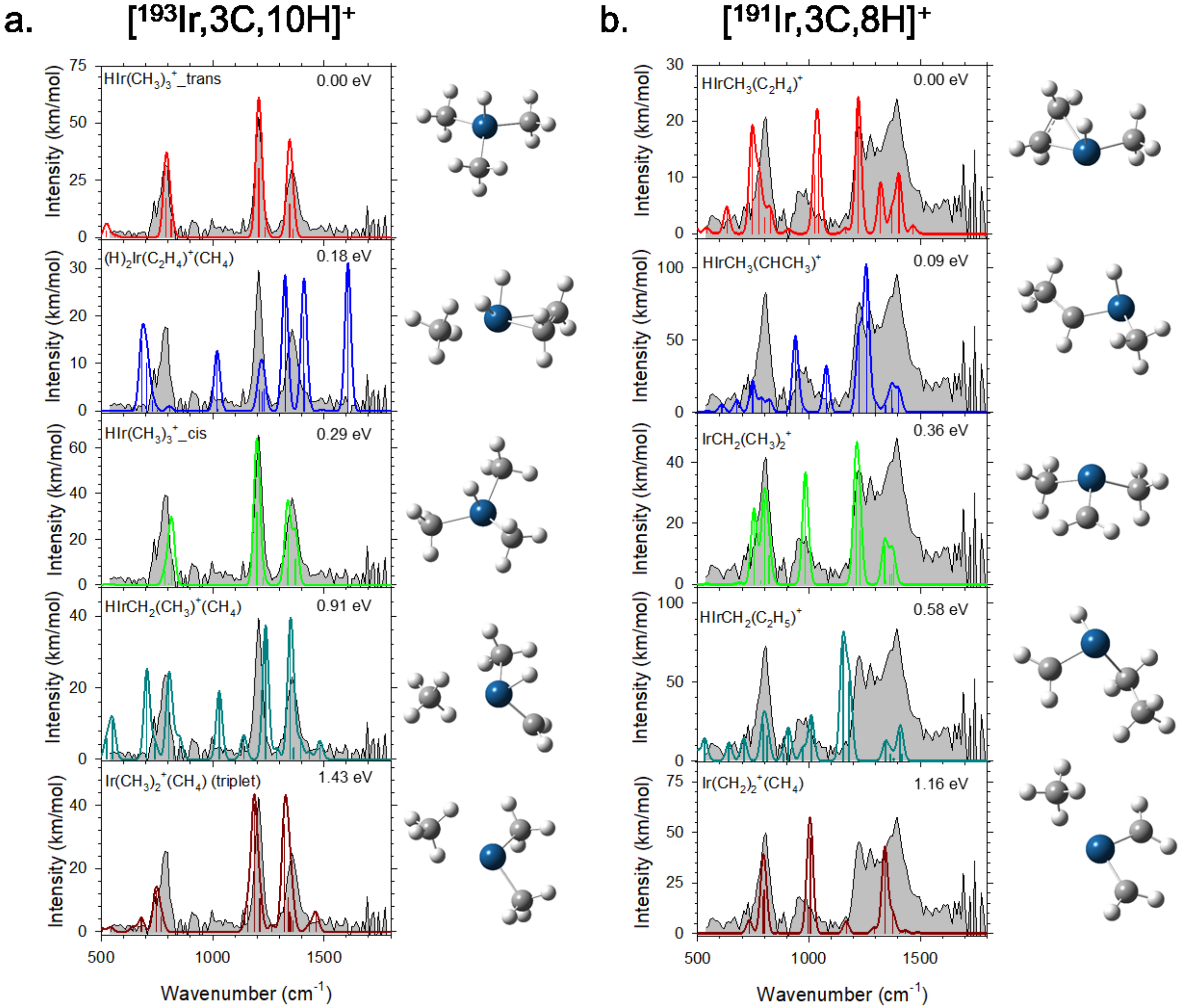
a.
[193Ir,3C,10H]+
b.
[191Ir,3C,8H]+
HIr(CH3)3+_trans
0.00 eV
(H)2Ir(C2H4)+(CH4)
0.18 eV
HIr(CH3)3+_cis
0.29 eV
HIrCH2(CH3)+(CH4)
0.91 eV
Ir(CH3)2+(CH4) (triplet)
1.43 eV
HIrCH3(C2H4)+
0.00 eV
HIrCH3(CHCH3)+
0.09 eV
IrCH2(CH3)2+
0.36 eV
HIrCH2(C2H5)+
0.58 eV
Ir(CH2)2+(CH4)
1.16 eV
Intensity (km/mol)
Wavenumber (cm-1)
500
1000
1500
0
25
50
75
10
20
30
40
60
100

Figure 2

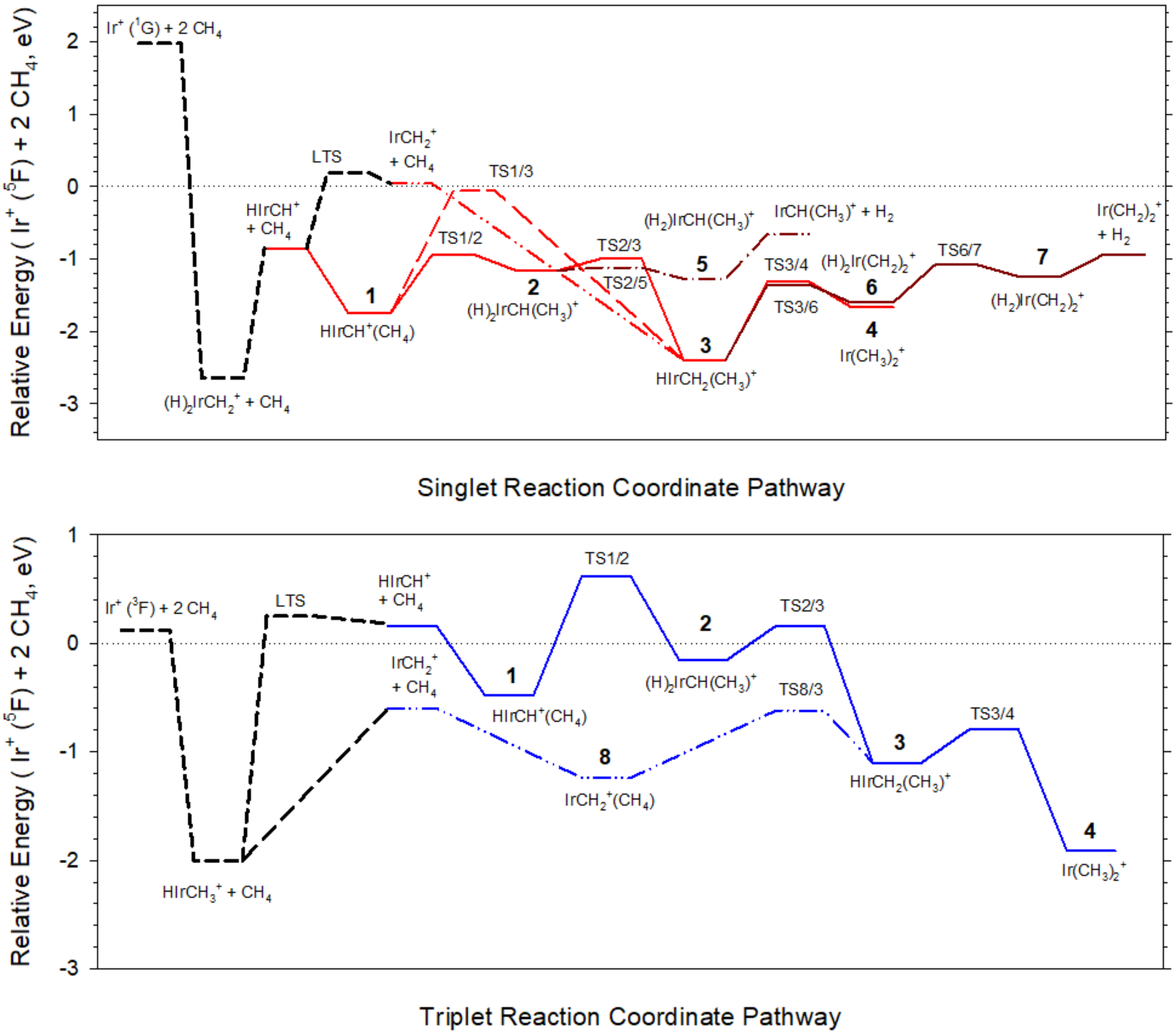
Relative Energy (Ir+ (5F) + 2 CH4, eV)
2
1
0
-1
-2
-3
Ir+ (1G) + 2 CH4
LTS
IrCH2+ + CH4
TS1/3
HIrCH+ + CH4
TS1/2
1
HIrCH+(CH4)
2
(H)2IrCH(CH3)+
TS2/3
TS2/5
(H2)IrCH(CH3)+
5
IrCH(CH3)+ + H2
3
HIrCH2(CH3)+
TS3/4
TS3/6
(H)2Ir(CH2)2+
6
4
Ir(CH3)2+
TS6/7
7
(H2)Ir(CH2)2+
Ir(CH2)2+ + H2
(H)2IrCH2+ + CH4
Singlet Reaction Coordinate Pathway
Relative Energy (Ir+ (5F) + 2 CH4, eV)
1
0
-1
-2
-3
Ir+ (3F) + 2 CH4
LTS
HIrCH+ + CH4
IrCH2+ + CH4
1
HIrCH+(CH4)
TS1/2
2
(H)2IrCH(CH3)+
TS2/3
TS8/3
8
IrCH2+(CH4)
3
HIrCH2(CH3)+
TS3/4
4
Ir(CH3)2+
HIrCH3+ + CH4
Triplet Reaction Coordinate Pathway

Figure 3

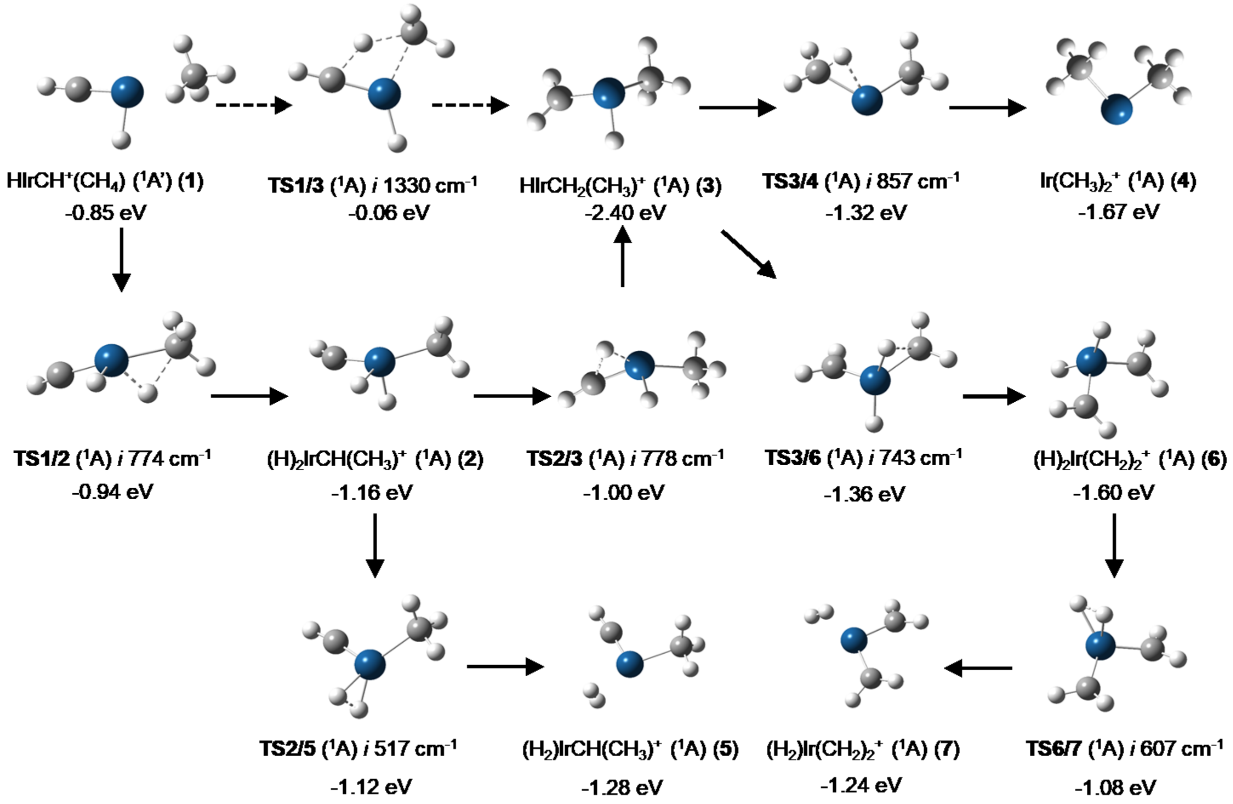
$HIrCH^+(CH_4)$ ($^1A'$) **(1)**
-0.85 eV
TS1/3 (^1A) *i* 1330 cm^{-1}
-0.06 eV
$HIrCH_2(CH_3)^+$ (^1A) **(3)**
-2.40 eV
TS3/4 (^1A) *i* 857 cm^{-1}
-1.32 eV
$Ir(CH_3)_2^+$ (^1A) **(4)**
-1.67 eV
TS1/2 (^1A) *i* 774 cm^{-1}
-0.94 eV
$(H)_2IrCH(CH_3)^+$ (^1A) **(2)**
-1.16 eV
TS2/3 (^1A) *i* 778 cm^{-1}
-1.00 eV
TS3/6 (^1A) *i* 743 cm^{-1}
-1.36 eV
$(H)_2Ir(CH_2)_2^+$ (^1A) **(6)**
-1.60 eV
TS2/5 (^1A) *i* 517 cm^{-1}
-1.12 eV
$(H_2)IrCH(CH_3)^+$ (^1A) **(5)**
-1.28 eV
$(H_2)Ir(CH_2)_2^+$ (^1A) **(7)**
-1.24 eV
TS6/7 (^1A) *i* 607 cm^{-1}
-1.08 eV

Figure 4

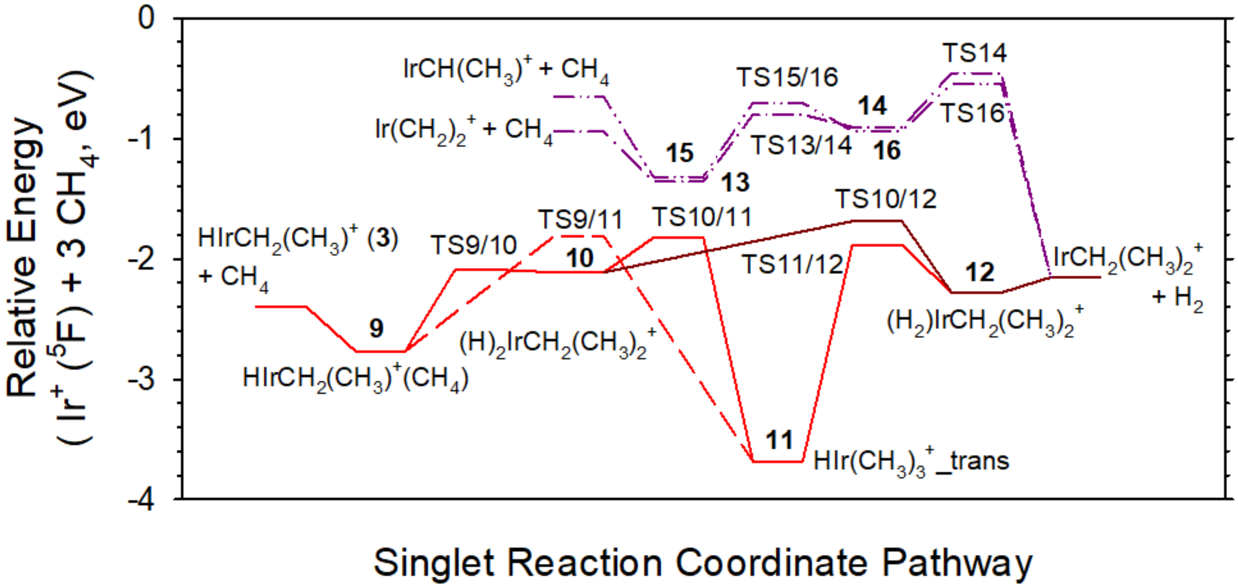
0
-1
-2
-3
-4
Relative Energy
(Ir$^+$ (^{5}F) + 3 CH$_4$, eV)
Singlet Reaction Coordinate Pathway
IrCH(CH$_3$)$^+$ + CH$_4$
Ir(CH$_2$)$_2$$^+$ + CH$_4$
TS15/16
TS14
14
TS16
15
TS13/14
16
13
TS9/11
TS10/11
TS10/12
HIrCH$_2$(CH$_3$)$^+$ (3)
+ CH$_4$
TS9/10
10
TS11/12
12
IrCH$_2$(CH$_3$)$_2$$^+$
+ H$_2$
9
(H)$_2$IrCH$_2$(CH$_3$)$_2$$^+$
(H$_2$)IrCH$_2$(CH$_3$)$_2$$^+$
HIrCH$_2$(CH$_3$)$^+$(CH$_4$)
11
HIr(CH$_3$)$_3$$^+$_trans

Figure 5

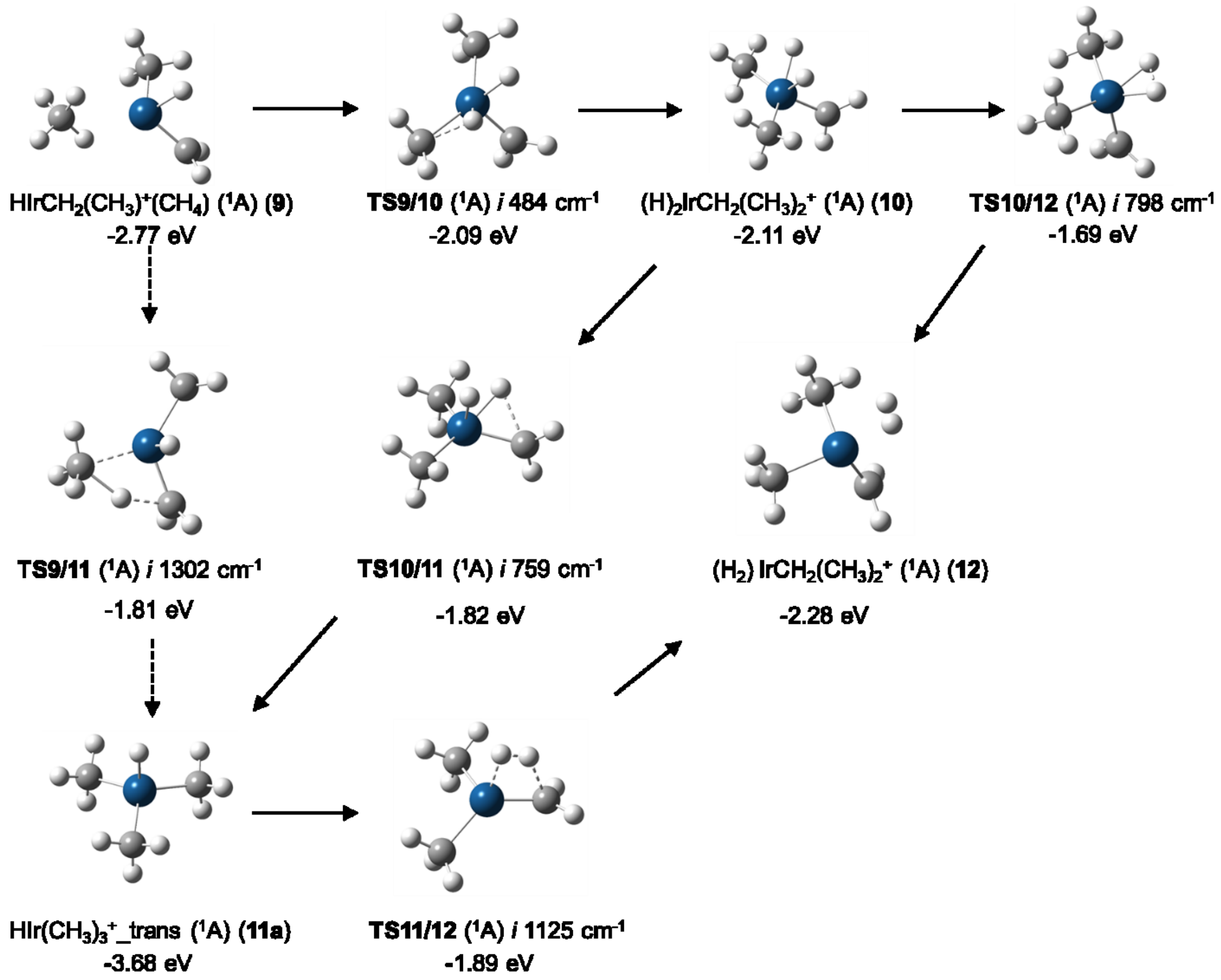

Figure 6

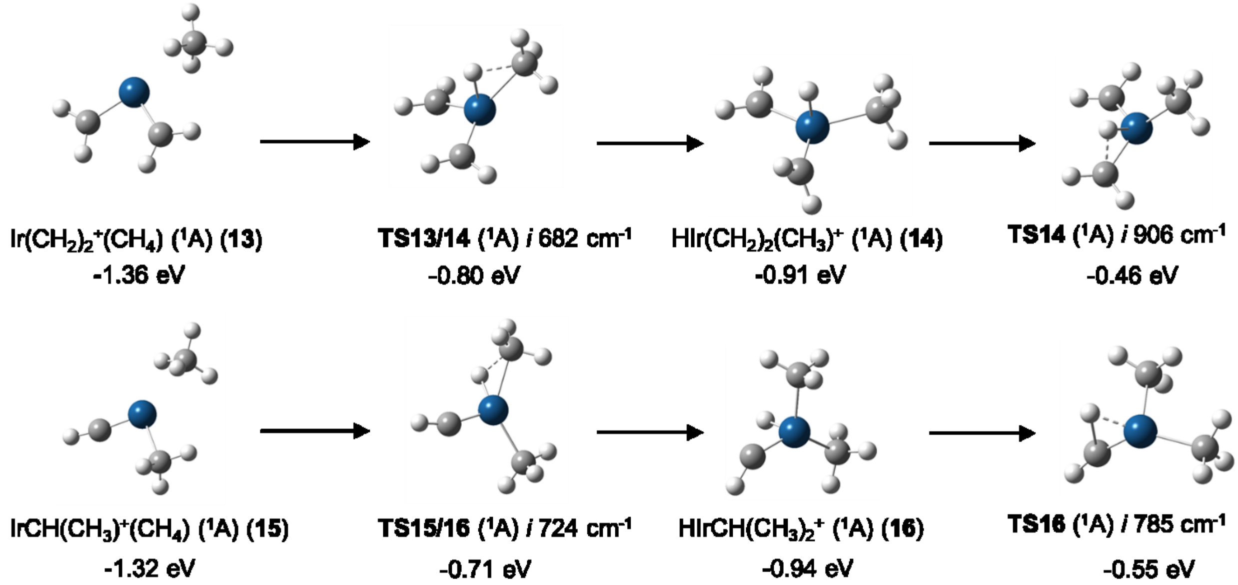

Figure 7

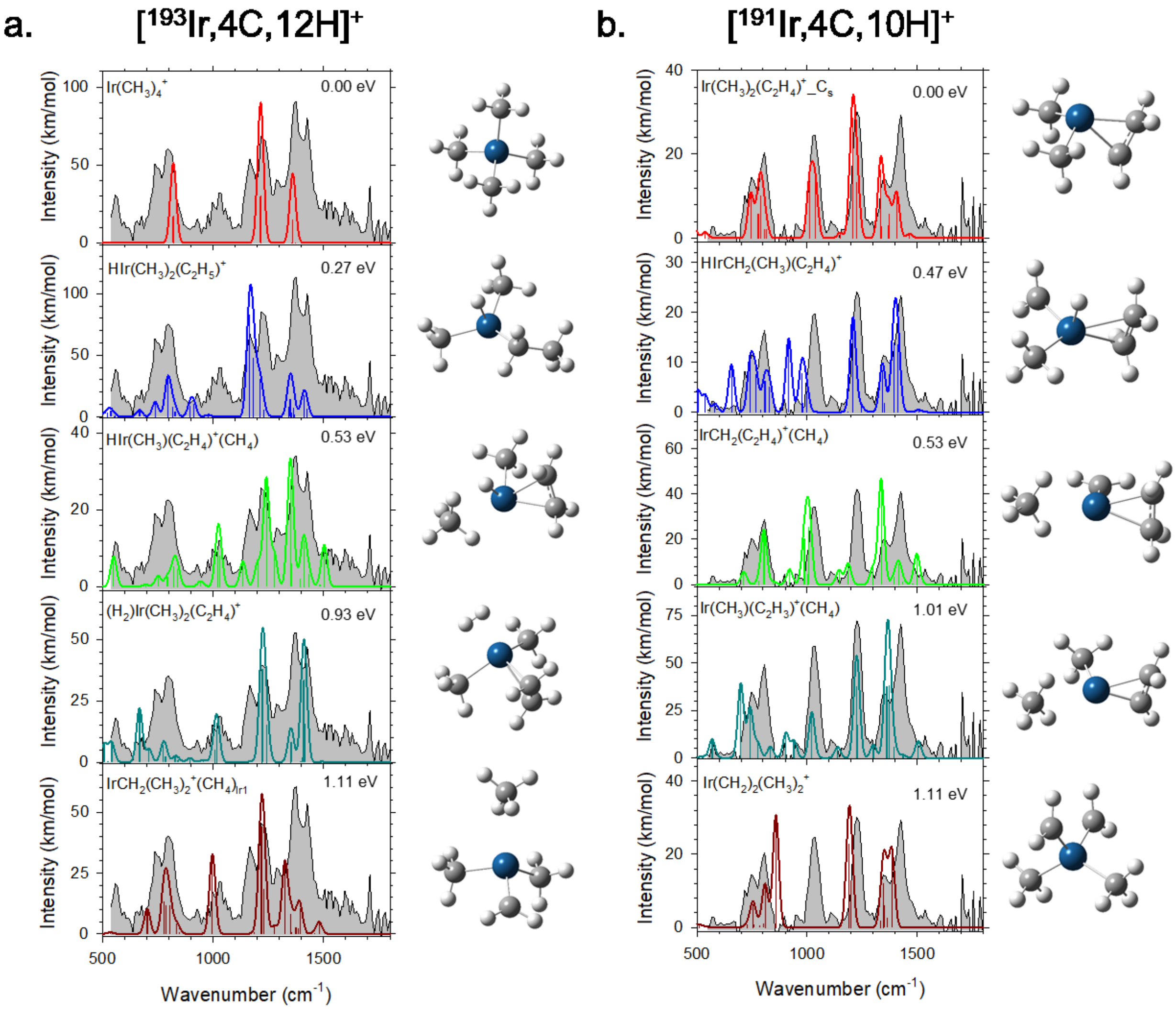
a.
$[^{193}Ir,4C,12H]^+$
b.
$[^{191}Ir,4C,10H]^+$
$Ir(CH_3)_4^+$
0.00 eV
$HIr(CH_3)_2(C_2H_5)^+$
0.27 eV
$HIr(CH_3)(C_2H_4)^+(CH_4)$
0.53 eV
$(H_2)Ir(CH_3)_2(C_2H_4)^+$
0.93 eV
$IrCH_2(CH_3)_2^+(CH_4)_{Ir1}$
1.11 eV
$Ir(CH_3)_2(C_2H_4)^+\_C_s$
0.00 eV
$HIrCH_2(CH_3)(C_2H_4)^+$
0.47 eV
$IrCH_2(C_2H_4)^+(CH_4)$
0.53 eV
$Ir(CH_3)(C_2H_3)^+(CH_4)$
1.01 eV
$Ir(CH_2)_2(CH_3)_2^+$
1.11 eV
Intensity (km/mol)
Wavenumber (cm^{-1})
500
1000
1500
0
25
50
75
100
10
20
30
40
60

Figure 8

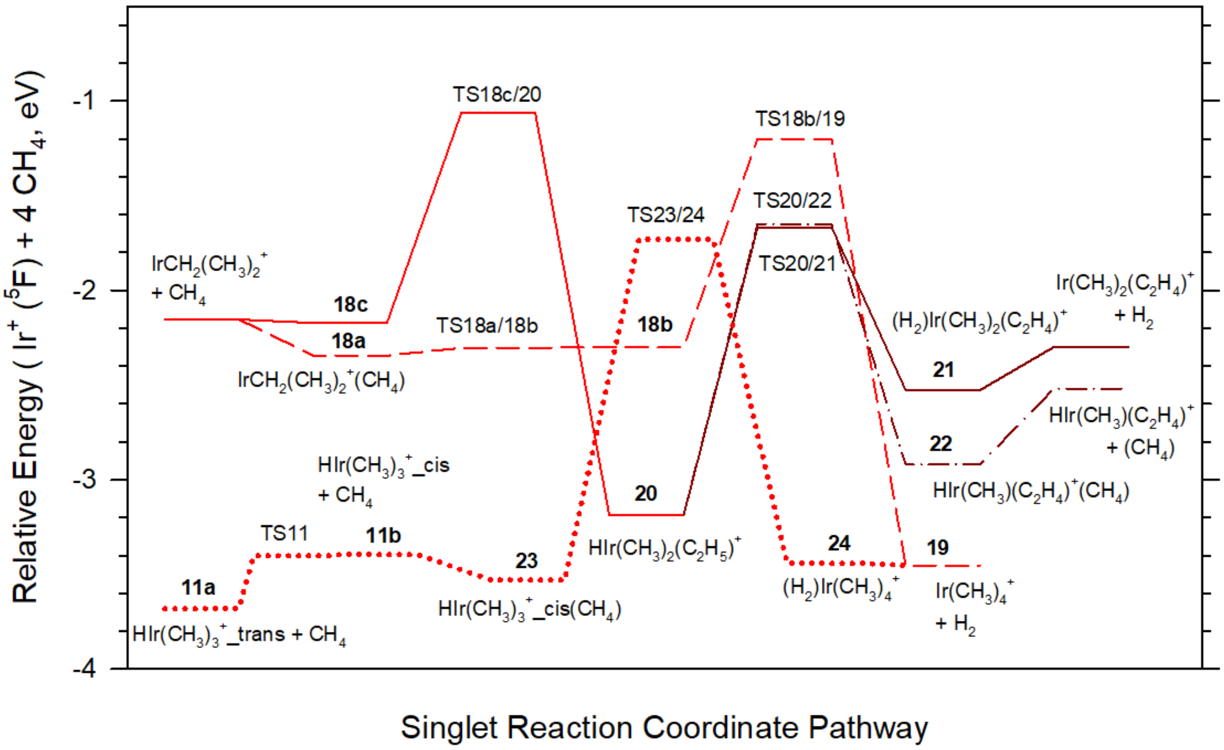
Relative Energy (Ir^+ (^5F) + 4 CH_4, eV)
-1
-2
-3
-4
Singlet Reaction Coordinate Pathway
TS18c/20
TS18b/19
TS20/22
TS23/24
TS20/21
$IrCH_2(CH_3)_2^+$ + CH_4
18c
18a
TS18a/18b
18b
$IrCH_2(CH_3)_2^+(CH_4)$
$Ir(CH_3)_2(C_2H_4)^+$ + H_2
$(H_2)Ir(CH_3)_2(C_2H_4)^+$
21
$HIr(CH_3)(C_2H_4)^+$ + (CH_4)
22
$HIr(CH_3)(C_2H_4)^+(CH_4)$
$HIr(CH_3)_3^+$_cis + CH_4
20
TS11
11b
23
$HIr(CH_3)_2(C_2H_5)^+$
24
19
11a
$(H_2)Ir(CH_3)_4^+$
$Ir(CH_3)_4^+$ + H_2
$HIr(CH_3)_3^+$_cis(CH_4)
$HIr(CH_3)_3^+$_trans + CH_4

Figure 9

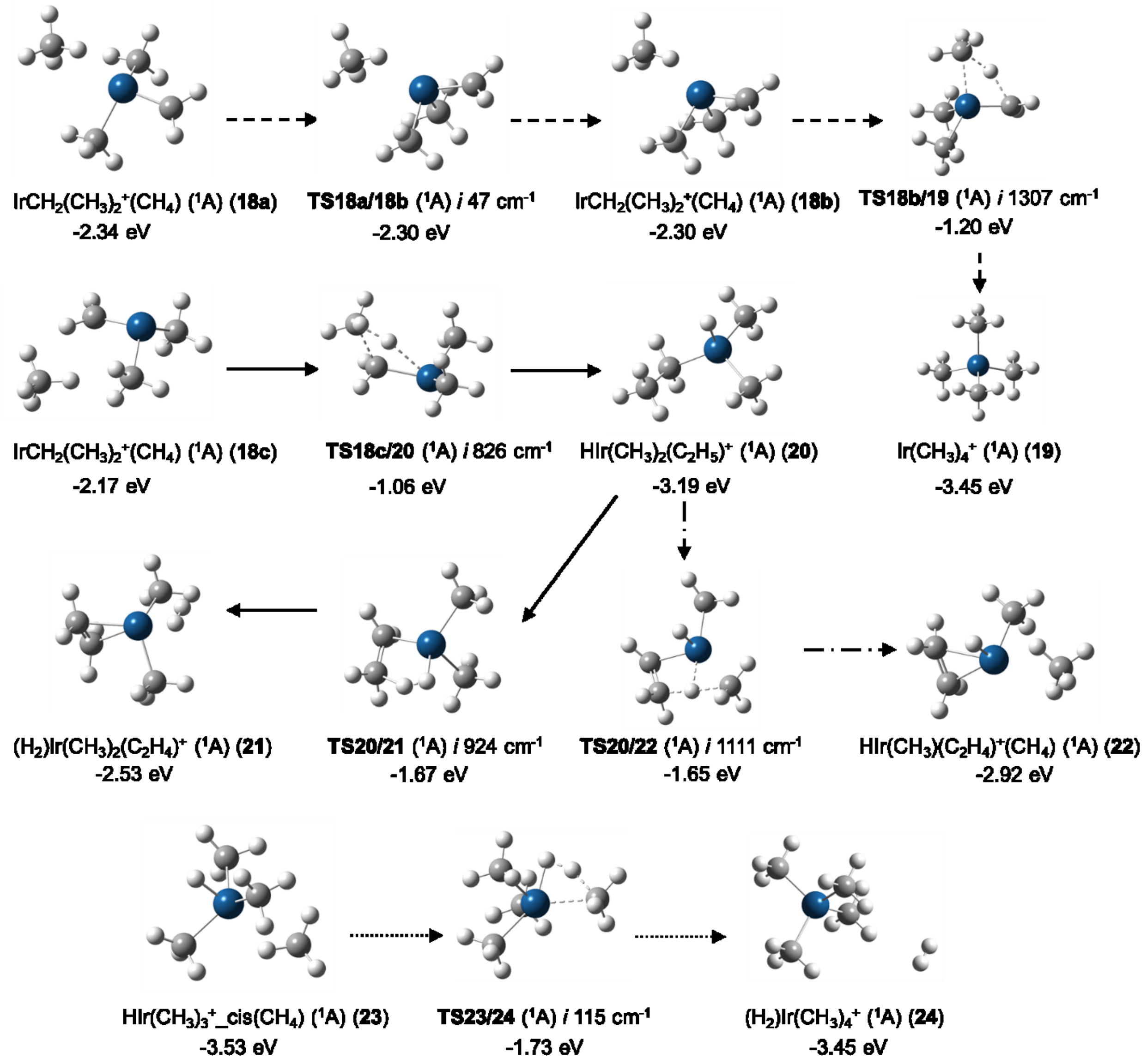
$IrCH_2(CH_3)_2^+(CH_4)$ (^1A) (**18a**)
-2.34 eV
TS18a/18b (^1A) *i* 47 cm^{-1}
-2.30 eV
$IrCH_2(CH_3)_2^+(CH_4)$ (^1A) (**18b**)
-2.30 eV
TS18b/19 (^1A) *i* 1307 cm^{-1}
-1.20 eV
$IrCH_2(CH_3)_2^+(CH_4)$ (^1A) (**18c**)
-2.17 eV
TS18c/20 (^1A) *i* 826 cm^{-1}
-1.06 eV
$HIr(CH_3)_2(C_2H_5)^+$ (^1A) (**20**)
-3.19 eV
$Ir(CH_3)_4^+$ (^1A) (**19**)
-3.45 eV
$(H_2)Ir(CH_3)_2(C_2H_4)^+$ (^1A) (**21**)
-2.53 eV
TS20/21 (^1A) *i* 924 cm^{-1}
-1.67 eV
TS20/22 (^1A) *i* 1111 cm^{-1}
-1.65 eV
$HIr(CH_3)(C_2H_4)^+(CH_4)$ (^1A) (**22**)
-2.92 eV
$HIr(CH_3)_3^+$_cis(CH_4) (^1A) (**23**)
-3.53 eV
TS23/24 (^1A) *i* 115 cm^{-1}
-1.73 eV
$(H_2)Ir(CH_3)_4^+$ (^1A) (**24**)
-3.45 eV

Figure 10